Three-Dimensional Thermo-Elasto-Hydrodynamic Computational Fluid Dynamics Model of a Tilting Pad Journal Bearing—Part II: Dynamic Response

Jongin Yang
Mem. ASME
Department of Mechanical Engineering,
Texas A&M University,
College Station, TX 77840
e-mail: jiyang@tamu.edu

Alan Palazzolo
James J. Cain Professor I
Fellow ASME
Department of Mechanical Engineering,
Texas A&M University,
College Station, TX 77840
e-mail: a-palazzolo@tamu.edu

Part II presents a novel approach for predicting dynamic coefficients for a tilting pad journal bearing (TPJB) using computational fluid dynamics (CFD) and finite element method (FEM), including fully coupled elastic deflection, heat transfer, and fluid dynamics. Part I presented a similarly novel, high fidelity approach for TPJB static response prediction which is a prerequisite for the dynamic characteristic determination. The static response establishes the equilibrium operating point values for eccentricity, attitude angle, deflections, temperatures, pressures, etc. The stiffness and damping coefficients are obtained by perturbing the pad and journal motions about this operating point to determine changes in forces and moments. The stiffness and damping coefficients are presented in "synchronously reduced form" as required by American Petroleum Institute (API) vibration standards. Similar to Part I, an advanced three-dimensional thermal—Reynolds equation code validates the CFD code for the special case when flow Between Pad (BP) regions is ignored, and the CFD and Reynolds pad boundary conditions are made identical. The results show excellent agreement for this validation case. Similar to the static response case, the dynamic characteristics from the Reynolds model show large discrepancies compared with the CFD results, depending on the Reynolds mixing coefficient (MC). The discrepancies are a concern given the key role that stiffness and damping coefficients serve instability and response predictions in rotordynamics software. The uncertainty of the MC and its significant influence on static and dynamic response predictions emphasizes a need to utilize the CFD approach for TPJB simulation in critical machines.
[DOI: 10.1115/1.4043350]

1 Introduction

The modeling of a tilting pad journal bearing (TPJB) for determining dynamic characteristics (coefficients) is a challenging task due to a large number of degrees-of-freedom involved, and the high sensitivity of the characteristics to thermal, hydrodynamic, and solid deformation influences. The coefficients ultimately become inputs to a rotordynamics system response code for determining the stability, critical speed, and forced responses of rotating machinery shafting. These codes typically have limitations on the form of the TPJB characteristics, limiting them to relating only x and y lateral motions and forces at a journal. The many degree of freedom TPJB model is therefore reduced to "equivalent" two degrees-of-freedom (2DOFs) form by assuming that all of the TPJB degrees-of-freedom move with a frequency specified by the analyst. Most often, this frequency is selected to be the shaft rotational speed frequency, in which case, the equivalent (2DOFs) coefficients are referred to as "synchronously reduced."

In 1964, Lund [1] first presented a method for solving the isoviscous Reynolds equation to obtain TPJB frequency reduced dynamic coefficients, assuming harmonic motions for the journal and pads. In 1987, Knight and Barrett [2] coupled a one-dimensional (1D) form of the energy equation with the Reynolds equation to provide a thermo-hydrodynamic modeling approach for TPJB dynamic characteristics. The shaft and pads were modeled as rigid against both thermal and hydrodynamic pressure loads. The mixing theory was adopted to estimate the inlet temperature of each pad, and the authors showed a high sensitivity of the dynamic coefficient with respect to the variation of oil supply temperature. In 1989, Brugier and Pascal [3] presented a TPJB model including a variable viscosity Reynolds equation coupled to a three-dimensional (3D) energy equation that assumed parabolically varying temperature through the film thickness at the pad inlet. Pad and pivot distortions were also included; however, the shaft temperature was assumed to be constant. The dynamic coefficients were obtained by slightly changing (perturbing) the shaft position and velocity around the equilibrium condition assuming that the temperatures and distortions remained constant. Pad deformation was shown to have a significant effect on the dynamic coefficients. Since then, the effects of pad deformation have been further investigated, and the modeling techniques have been further developed by other researchers [4–7]. Recently in 2015, Suh and Palazzolo [8] presented a new modeling method for the 3D thermo-elasto-hydrodynamic of a TPJB. The generalized Reynolds and 3D energy equations were employed, along with pivot flexibility and shaft and pad heat conduction with effects on distortions. Mixing theory with mixing coefficients (MCs) was applied at the boundaries of the energy equation between the pads. A modal coordinate transformation was utilized in the flexible pad dynamic model to reduce computation time.

Contributed by the Tribology Division of ASME for publication in the Journal of Tribology. Manuscript received October 26, 2018; final manuscript received March 27, 2019; published online April 30, 2019. Assoc. Editor: Stephen Boedo.

As discussed in Part I, the uncertainty of the MC leads to uncertainty of the inlet temperature boundary conditions on the pads and on all calculated quantities, such as peak pad temperature, drag torque, etc. The present computational fluid dynamics (CFD) approach eliminates the uncertainty associated with the MC by including a detailed flow and thermal model in the volumes between pads. Publications of research on applying CFD to obtain the dynamic characteristics of TPJB are pause.

In 2005, Guo et al. [9] presented a CFD modeling technique for the fixed pad, hydrodynamic and hydrostatic, bearings with the oil inlet geometry, considering the Navier–Stokes and energy equations. Stiffness coefficients were obtained by imposing perturbations of the shaft position, and damping coefficients were calculated by utilizing the moving grid function in a commercial code. In 2008, Meruane and Pascual [10] presented a transient, 3D, fluid–structure interaction (FSI), CFD model of a plain journal bearing to determine nonlinear, rotor transient response under various operating conditions. A numerical approach was developed to obtain the nonlinear dynamic coefficients of a Taylor series force model, including both displacement and velocity perturbations. The transient CFD modeling technique has been further developed in Refs. [11–13] to predict the nonlinear dynamic behavior of rotors supported in fluid film journal bearings. Reference [13] included thermal and elastic deformations of the shaft and fixed pads, a flexible rotor, and detailed oil inlet geometry. They did not consider tilt pad bearings or the calculation of stiffness and damping coefficients. The modeling of a TPJB to determine stiffness and damping coefficients employing a CFD-FSI approach has not been reported until the present work.

The approach presented here is the first model of a TPJB including 3D-CFD with multiphase flow, thermal–fluid interaction, transitional turbulence, convective term in the energy equation due to shaft spin, pivot flexibility, and thermal distortions of the mechanical system by two-way FSI modeling. Part II builds on the static equilibrium model presented in Part I, by presenting a detailed modeling approach for obtaining frequency reduced dynamic coefficients, and log decrement for rotordynamic response of a Jeffcott rotor. The dynamic coefficients of the proposed CFD model are also compared with the results of a high fidelity Reynolds model, which, as illustrated in Part I for the static response, have significant variability due to the uncertainty of the MCs. Thus, the CFD approach presented may provide significant benefits in improving accuracy for predicting dynamic coefficients of a TPJB.

The main contributions of this paper include:

(a) A TPJB modeling methodology that includes a CFD solution of the Navier–Stokes and energy equations between pads for predicting dynamic force coefficients.
(b) Investigation of the effect of MC uncertainty on the TPJB dynamic force coefficient predictions, with a comparison to CFD predictions.
(c) Results demonstrating that the conventional Reynolds—MC approach may yield dynamic force coefficients that significantly differ from those obtained by a higher fidelity CFD model, even if the former utilizes a very wide range of MC.

2 Description of Fluid–Structure Interaction—Computational Fluid Dynamics Model

2.1 Overall Description. Determination of the static response of the TPJB including temperatures, pressures, eccentricity, attitude angle, etc., as illustrated in Part I, is a necessary prerequisite for obtaining the dynamic response characteristics. The geometry and meshing are for the most part preserved from the static to the dynamic response model. Figure 1 provides assembled and exploded views of the TPJB geometry and modeling domains.

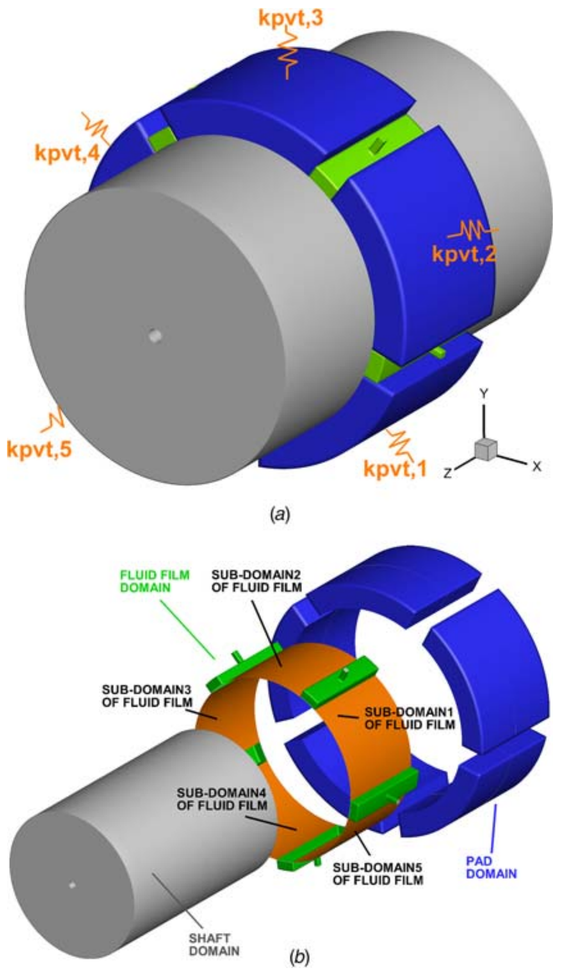

(a)

(b)

Fig. 1 Configuration of tilting pad journal bearing model: (*a*) overview and (*b*) exploded view

The subdomains in the fluid film domain are newly defined for prescribing the perturbed velocity source term of the transport equations, which is used for calculating the damping coefficients. Source terms in the governing equations due to the velocity perturbations arise only in these subdomains and not in the BP regions. Displacement perturbations for obtaining stiffness coefficients do not contribute source terms but instead modify the film thickness distributions. Major simulation steps for the dynamics response stage include hydrodynamic force and moment determination with the CFD-solver, dynamic coefficient evaluation using a MATLAB code, and iteration control with a Job Script. These steps are repeated for all coordinate perturbations in determining the full set of dynamic coefficients (stiffness and damping).

Figure 2 shows a flow diagram of the computational solution process for obtaining TPJB dynamic force characteristics (coefficients) via FSI modeling. The pads and journal are considered rigid for the small perturbation dynamic analysis, although they deflect in the static analysis. The perturbations are taken about a static equilibrium state that is obtained by the methods provided in Part I. All of the static equilibrium values of the dependent variables including the equilibrium positions of the shaft and pads are loaded into the CFD-solver, prior to starting the CFD solution for the dynamics case. The dynamic system model's CFD solution solves the same equations as in the static system solution. Thus, the CFD-solver includes incompressible multiphase flow, transitional turbulence, and thermal–fluid interaction with variable viscosity in the fluid film domain. Two key differences occur between the static (Part I) and dynamic (Part II) models in the FSI solver. The first is that the temperature distribution of the solid domain is assumed to remain constant during a coordinate perturbation. This temperature distribution is obtained from the static calculation and is forced to remain constant by imposing a 0 timescale factor in the energy equation. This is a reasonable assumption

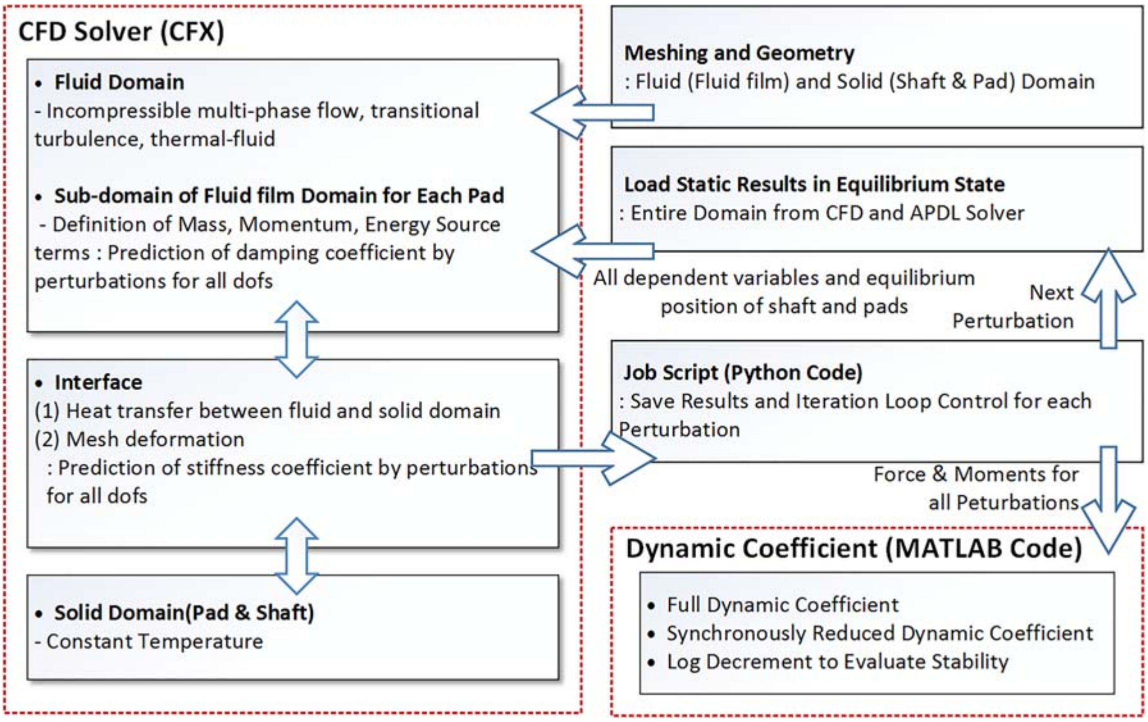

Fig. 2 Flow diagram of CFD-based FSI TPJB modeling for dynamic performance prediction

due to the thermal time constants being much longer than the pressure time constants resulting from the coordinate perturbations. The second difference is that the perturbed displacements at the interface boundaries between the shaft-pad and fluid film and the corresponding perturbed velocity source terms of the transport equations need to be considered for each subdomain, when calculating the full set of dynamic coefficients. The Job Script controls the iteration procedure while accumulating and saving the results for each coordinate perturbation. The results provide the pressure induced reaction forces acting on the shaft, and the moments acting on the pads. These results are transferred to the MATLAB code after completing all perturbation related computations. The MATLAB code determines the full set of dynamic coefficients, which are then synchronously reduced. This is the form commonly used and required by the American Petroleum Institute (API) compressor standard, for evaluating the rotordynamic stability of a TPJB supported rotor via its predicted log decrements.

2.2 Full Dynamic Coefficient Matrices

2.2.1 Stiffness Matrix. The full stiffness coefficient matrix is obtained by imposing displacement and angular perturbations $(\Delta \boldsymbol{x}_{pb}{}^T, \Delta \boldsymbol{y}_{pb}{}^T, \Delta \boldsymbol{\delta}_{pb}{}^T, \Delta \boldsymbol{p}_{pb}{}^T)$ relative to the static equilibrium state, as shown in Fig. 3. The illustrative example TPJB has five pads, so it has 12 degrees-of-freedom, including two journal displacements, five pad rotations, and five pivot displacements. Each degree of freedom is perturbed in both positive and negative directions relative to the static equilibrium, yielding a total of 24 perturbations to obtain the full stiffness matrix. The magnitudes of the finite perturbations are selected to balance the need for obtaining a numerically reliable change in force or moment, while accurately approximating the definition of stiffness as representing a slope at a point.

The magnitude of the perturbations is chosen from numerical tests as $0.01C_{l,b}$ for the translational perturbations and 0.001 deg for the angular perturbations.

The perturbation related displacements are added to the static equilibrium counterparts to form "total" displacement equations. These equations are imposed at the interface boundaries between the shaft-pad and fluid film to solve the mesh deformation equation

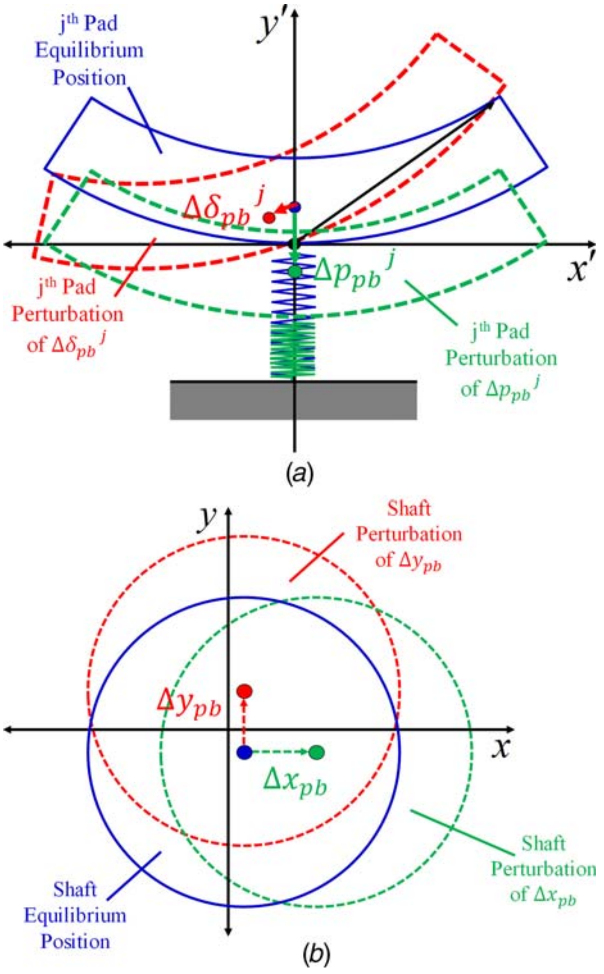

Fig. 3 TPJB perturbations for stiffness: (*a*) pivot displacement and pad angle of the *j*th pad and (*b*) *x* and *y* journal displacements

for the perturbation. The total perturbed displacement equations are applied at the interface boundaries and are derived from the film thickness expressions. These allow mesh deformation only in the radial direction, which conserves the orthogonal quality of the mesh to improve convergence characteristics. The derivation of the equations proceeds from the film thickness at the equilibrium state as

$$h_e{}^j(\theta)=\{C_{l,p}{}^j-(C_{l,p}{}^j-C_{l,b})\cos(\theta-\theta_p{}^j)\}-\{x_{se}-p_e{}^j\cos(\theta_p{}^j)\}\cos(\theta)$$
$$-\{y_{se}-p_e{}^j\sin(\theta_p{}^j)\}\sin(\theta)-\delta_e{}^jR_s\sin(\theta-\theta_p{}^j)-h_{s,TEe}-h_{p,TEe} \tag{1}$$

Figure 4 illustrates the parameters used in Eq. (1)

$$h_e^j,\ \theta,\ \theta_p{}^j,\ x_{se},\ y_{se},\ p_e{}^j,\ \delta_e{}^j,\ h_{s,TEe},\ h_{p,TEe},\ R_s$$

The first term is disregarded in the perturbation simulations since it corresponds to the baseline geometry and mesh incorporating the preload, bearing clearance, and pad clearance, when all displacements of the TPJB are zero. The relative change of the film thickness with respect to the equilibrium state, due to perturbations of the pad and shaft motions is expressed in terms of the angular coordinate θ as

$$\Delta h_p^j(\theta)=\Delta p_{pb}{}^j\cos(\theta_p^j)\cos(\theta)+\Delta p_{pb}{}^j\sin(\theta_p{}^j)\sin(\theta)$$
$$-\Delta\delta_{pb}{}^jR_s\sin(\theta-\theta_p^j) \tag{2}$$

$$\Delta h_s(\theta)=-\Delta x_{pb}\cos(\theta)-\Delta y_{pb}\sin(\theta) \tag{3}$$

The global coordinate x and y displacements of the pad and shaft surfaces, relative to equilibrium, vary with angular coordinate θ and the incremental film thicknesses in Eqs. (2) and (3).

Pad tilting and pivot motion displacements (θ):

$$\Delta x_p{}^j(\theta)=\Delta h_p{}^j(\theta)\cos(\theta) \tag{4}$$

$$\Delta y_p{}^j(\theta)=\Delta h_p{}^j(\theta)\sin(\theta) \tag{5}$$

Shaft translational motion displacement (θ):

$$\Delta x_s(\theta)=\Delta h_s(\theta)\cos(\theta) \tag{6}$$

$$\Delta y_s(\theta)=\Delta h_s(\theta)\sin(\theta) \tag{7}$$

Substitution of Eqs. (2) and (3) into Eqs. (4)–(7) yields expressions for pad and shaft surface displacements relative to the equilibrium state in terms of the pivot displacements, journal displacements, and pad angles relative to the equilibrium state and the angular coordinate θ.

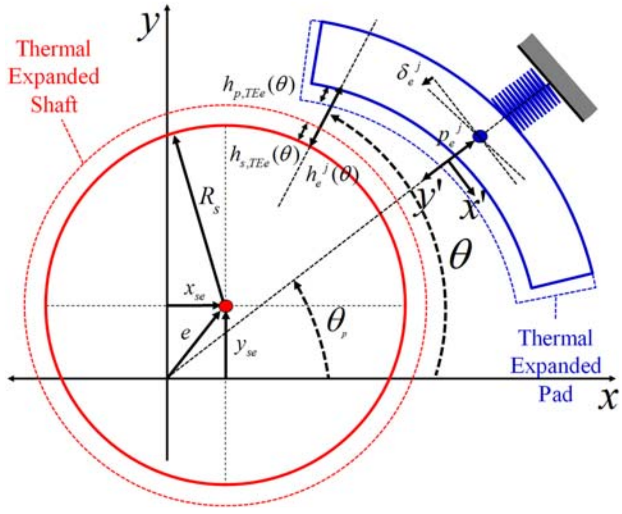

Fig. 4 Illustration of film thickness parameters at the equilibrium condition

Pad tilting and pivot motion displacements (θ):

$$\Delta x_p{}^j(\theta)=\{\Delta p_{pb}{}^j\cos(\theta_p{}^j)\cos(\theta)+\Delta p_{pb}{}^j\sin(\theta_p{}^j)\sin(\theta)$$
$$-\Delta\delta_{pb}{}^jR_s\sin(\theta-\theta_p{}^j)\}\cos(\theta) \tag{8}$$

$$\Delta y_p^j(\theta)=\{\Delta p_{pb}{}^j\cos(\theta_p^j)\cos(\theta)+\Delta p_{pb}{}^j\sin(\theta_p^j)\sin(\theta)$$
$$-\Delta\delta_{pb}{}^jR_s\sin(\theta-\theta_p^j)\}\sin(\theta) \tag{9}$$

Shaft translational motion displacement (θ):

$$\Delta x_s(\theta)=\{-\Delta x_{pb}\cos(\theta)-\Delta y_{pb}\sin(\theta)\}\cos(\theta) \tag{10}$$

$$\Delta y_s(\theta)=\{-\Delta x_{pb}\cos(\theta)-\Delta y_{pb}\sin(\theta)\}\sin(\theta) \tag{11}$$

The initial x and y coordinate (x_0, y_0) of the nodes at shaft-film and pad-film interface boundaries are approximately

$$x_0\simeq R_s\cos(\theta) \tag{12}$$

$$y_0\simeq R_s\sin(\theta) \tag{13}$$

where the very thin-film thickness between the shaft and pads has been neglected. Equations (12) and (13) are solved for $\cos(\theta)$ and $\sin(\theta)$, which are then substituted into Eqs. (8)–(11) to obtain

Total perturbed displacements of the pad surface due to pad tilting and pivot displacements:

$$\Delta x_{p,totp}{}^j(x,y)=\left\{-\frac{\Delta\delta_{pb}{}^j}{R_s}x_0(y_0\cos\theta_p^j-x_0\sin\theta_p^j)\right\}$$
$$+\left\{\frac{\Delta p_{pb}{}^j}{R_s^2}x_0(x_0\cos\theta_p^j+y_0\sin\theta_p^j)\right\} \tag{14}$$

$$\Delta y_{p,totp}{}^j(x,y)=\left\{-\frac{\Delta\delta_{pb}{}^j}{R_s}y_0(y_0\cos\theta_p{}^j-x_0\sin\theta_p{}^j)\right\}$$
$$+\left\{\frac{\Delta p_{pb}{}^j}{R_s{}^2}y_0(x_0\cos\theta_p{}^j+y_0\sin\theta_p{}^j)\right\} \tag{15}$$

Total perturbed displacements of the journal surface due to shaft translational displacements:

$$\Delta x_{s,totp}(x,y)=\frac{x_0}{R_s^2}(\Delta x_{pb}x_0+\Delta y_{pb}y_0) \tag{16}$$

$$\Delta y_{s,totp}(x,y)=\frac{y_0}{R_s^2}(\Delta x_{pb}x_0+\Delta y_{pb}y_0) \tag{17}$$

Equations (14)–(17) provide the change in the pad and journal nodal coordinates that result from perturbing the journal, pads, and pivots.

The displacements for each perturbation are imposed on the fluid film interface boundaries in the CFD model, which solves for pressures, forces, and moments needed to determine the stiffness and damping coefficients.

Displacements in the z-direction are ignored due to their minor influence on the film thickness and for the preservation of the mesh's (orthogonal) quality. Each component perturbation is substituted to the total perturbed displacement equations in order. The total perturbation displacement of the shaft and pad motions is applied at the interface boundaries between the shaft-pad and fluid film. The resulting pressure distributions are then used to obtain pad moments and reaction forces on the shaft and pad. The moments and forces are then utilized to calculate the full stiffness coefficient matrix, defined as follows:

$$\left[k_{brg}\right]=\left[\begin{array}{c:c}\mathbf{k}_{JJ} & \mathbf{k}_{JP}\\ \hdashline \mathbf{k}_{PJ} & \mathbf{k}_{PP}\end{array}\right]=\left[\begin{array}{c:c:c:c}k_{xx} & k_{xy} & \mathbf{k}_{x\delta} & \mathbf{k}_{xp}\\ \hdashline k_{yx} & k_{yy} & \mathbf{k}_{y\delta} & \mathbf{k}_{yp}\\ \hdashline \mathbf{k}_{\delta x} & \mathbf{k}_{\delta y} & \mathbf{k}_{\delta\delta} & \mathbf{k}_{\delta p}\\ \hdashline \mathbf{k}_{px} & \mathbf{k}_{py} & \mathbf{k}_{p\delta} & \mathbf{k}_{pp}\end{array}\right] \tag{18}$$

$$k_{xx}=-\frac{F_{s,x}(+\Delta x_{pb})-F_{s,x}(-\Delta x_{pb})}{2\Delta x_{pb}} \tag{19}$$

$$k_{yx}=-\frac{F_{s,y}(+\Delta x_{pb})-F_{s,y}(-\Delta x_{pb})}{2\Delta x_{pb}} \tag{20}$$

$$k_{\delta^j x}=-\frac{M_p{}^j(+\Delta x_{pb})-M_p{}^j(-\Delta x_{pb})}{2\Delta x_{pb}},\ \text{term in }\mathbf{k}_{\delta x}\text{ Eq. (18)} \tag{21}$$

$$k_{p^j x}=-\frac{F_p{}^j(+\Delta x_{pb})-F_p{}^j(-\Delta x_{pb})}{2\Delta x_{pb}},\ \text{term in }\mathbf{k}_{px}\text{ in Eq. (18)} \tag{22}$$

$$k_{xy}=-\frac{F_{s,x}(+\Delta y_{pb})-F_{s,x}(-\Delta y_{pb})}{2\Delta y_{pb}} \tag{23}$$

$$k_{yy}=-\frac{F_{s,y}(+\Delta y_{pb})-F_{s,y}(-\Delta y_{pb})}{2\Delta y_{pb}} \tag{24}$$

$$k_{\delta^j y}=-\frac{M_p{}^j(+\Delta y_{pb})-M_p{}^j(-\Delta y_{pb})}{2\Delta y_{pb}},\ \text{term in }\mathbf{k}_{\delta y}\text{ in Eq. (18)} \tag{25}$$

$$k_{p^j y}=-\frac{F_p{}^j(+\Delta y_{pb})-F_p{}^j(-\Delta y_{pb})}{2\Delta y_{pb}},\ \text{term in }\mathbf{k}_{py}\text{ in Eq. (18)} \tag{26}$$

$$k_{x\delta^j}=-\frac{F_{s,x}(+\Delta\delta_{pb}{}^j)-F_{s,x}(-\Delta\delta_{pb}{}^j)}{2\Delta\delta_{pb}{}^j},\ \text{term in }\mathbf{k}_{x\delta}\text{ in Eq. (18)} \tag{27}$$

$$k_{y\delta^j}=-\frac{F_{s,y}(+\Delta\delta_{pb}{}^j)-F_{s,y}(-\Delta\delta_{pb}{}^j)}{2\Delta\delta_{pb}{}^j},\ \text{term in }\mathbf{k}_{y\delta}\text{ in Eq. (18)} \tag{28}$$

$$k_{\delta^i\delta^j}=-\frac{M_p{}^i(+\Delta\delta_{pb}{}^j)-M_p{}^i(-\Delta\delta_{pb}{}^j)}{2\Delta\delta_{pb}{}^j},\ \text{term in }\mathbf{k}_{\delta\delta}\text{ in Eq. (18)} \tag{29}$$

$$k_{p^i\delta^j}=-\frac{F_p{}^i(+\Delta\delta_{pb}{}^j)-F_p{}^i(-\Delta\delta_{pb}{}^j)}{2\Delta\delta_{pb}{}^j},\ \text{term in }\mathbf{k}_{p\delta}\text{ in Eq. (18)} \tag{30}$$

$$k_{xp}{}^j=-\frac{F_{s,x}(+\Delta p_{pb}{}^j)-F_{s,x}(-\Delta p_{pb}{}^j)}{2\Delta p_{pb}{}^j},\ \text{term in }\mathbf{k}_{xp}\text{ in Eq. (18)} \tag{31}$$

$$k_{yp}{}^j=-\frac{F_{s,y}(+\Delta p_{pb}{}^j)-F_{s,y}(-\Delta p_{pb}{}^j)}{2\Delta p_{pb}{}^j},\ \text{term in }\mathbf{k}_{yp}\text{ in Eq. (18)} \tag{32}$$

$$k_{\delta^i p^j}=-\frac{M_p{}^i(+\Delta p_{pb}{}^j)-M_p{}^i(-\Delta p_{pb}{}^j)}{2\Delta p_{pb}{}^j},\ \text{term in }\mathbf{k}_{\delta p}\text{ in Eq. (18)} \tag{33}$$

$$\begin{aligned}k_{p^i p^j}=&-\frac{F_p{}^i(+\Delta p_{pb}{}^j)-F_p{}^i(-\Delta p_{pb}{}^j)}{2\Delta p_{pb}{}^j}\\ &-\frac{F_{pvt}{}^i(+\Delta p_{pb}{}^j)-F_{pvt}{}^i(-\Delta p_{pb}{}^j)}{2\Delta p_{pb}{}^j},\ \text{term in }\mathbf{k}_{pp}\end{aligned} \tag{34}$$

2.2.2 Damping Coefficient. The full damping coefficient matrix can be obtained from velocity perturbations ($\Delta\dot{\boldsymbol{x}}_{pb}{}^T$, $\Delta\dot{\boldsymbol{y}}_{pb}{}^T$, $\Delta\dot{\boldsymbol{\delta}}_{pb}{}^T$, $\Delta\dot{\boldsymbol{p}}^T_{pb}$) of the shaft and pad degrees-of-freedom, similar to the calculation of stiffness coefficients from position perturbations. This requires 24 perturbations, involving both positive and negative movements. The magnitude of the velocity perturbation is $0.01C_{l,b}\Omega_s$ for translational velocity perturbations and 0.001 deg Ω_s for angular velocity perturbations. The velocity perturbations are substituted into the perturbed velocity source terms of the transport equations in the defined subdomains of the fluid film (Fig. 1). The transport equations are the continuity, momentum, and energy conservation equations in Eqs. (35), (37), and (39), respectively. The perturbed velocity source term for each transport equation can be written as given in Eqs. (36), (38), and (40), assuming that the sources from the velocity perturbation are distributed uniformly through the film thickness.

Continuity equation with the perturbed velocity source term:

$$\frac{\partial}{\partial x_i}(\rho_f u_i)=\sum_j s_C{}^j \tag{35}$$

$$\frac{s_C{}^j=-\partial\rho_f{}^j}{\partial t}\simeq-\left(\frac{\rho_l}{h_e^j}\frac{\partial h_e{}^j(x,y,z)}{\partial t}r_l+\frac{\rho_v}{h_e^j}\frac{\partial h_e{}^j(x,y,z)}{\partial t}(1-r_l)\right) \tag{36}$$

Momentum equation with the perturbed velocity source term:

$$\frac{\partial}{\partial x_j}(\rho_f u_i u_j)=-\frac{\partial p'}{\partial x_i}+\frac{\partial}{\partial x_j}\left[\mu_{eff}\left(\frac{\partial u_i}{\partial x_j}+\frac{\partial u_j}{\partial x_i}\right)\right]+\sum_j s_M{}^j \tag{37}$$

$$\frac{s_M{}^j=-\partial\rho_f u_i{}^j}{\partial t}\simeq-\left(\frac{\rho_l u_i}{h_e^j}\frac{\partial h_e{}^j(x,y,z)}{\partial t}r_l+\frac{\rho_v u_i}{h_e^j}\frac{\partial h_e{}^j(x,y,z)}{\partial t}(1-r_l)\right) \tag{38}$$

Energy equation with the perturbed velocity source term:

$$\begin{aligned}-\frac{\partial p}{\partial t}+\frac{\partial}{\partial x_j}(\rho_f u_j h_{tot})=&\frac{\partial}{\partial x_j}\left(\lambda_f\frac{\partial T_f}{\partial x_j}+\frac{\mu_t}{\mathrm{Pr}_t}\frac{\partial h_f}{\partial x_j}\right)+\frac{\partial}{\partial x_j}[u_i(\tau_{ij}-\rho_f\overline{u_i u_j})]\\ &+\sum_j s_E{}^j\end{aligned} \tag{39}$$

$$\frac{s_E{}^j=-\partial\rho_f h_{tot}{}^j}{\partial t}\simeq-\left(\frac{\rho_l C_p T_f}{h_e^j}\frac{\partial h_e{}^j(x,y,z)}{\partial t}r_l+\frac{\rho_v C_p T_f}{h_e^j}\frac{\partial h_e{}^j(x,y,z)}{\partial t}(1-r_l)\right) \tag{40}$$

where $h_e{}^j$ is the film thickness in the equilibrium condition. This is defined after a coordinate transformation to the x–y coordinates as

$$\begin{aligned}h_e{}^j(x,y,z)=&\,C_{l,p}{}^j-\frac{(C_{l,p}-C_{l,b})}{R_s}\{x_0\cos(\theta_p{}^j)+y_0\sin(\theta_p{}^j)\}\\ &-\frac{1}{R_s}[\{x_{se}-p_e{}^j\cos(\theta_p{}^j)\}x_0+\{y_{se}-p_e{}^j\sin(\theta_p{}^j)\}y_0]\\ &-\delta_e{}^j\{y_0\cos(\theta_p{}^j)-x_0\sin(\theta_p{}^j)\}-h_{s,TEe}(x_0,y_0,z_0)\\ &-h_{p,TEe}(x_0,y_0,z_0)\end{aligned} \tag{41}$$

where

$$h_{s,TEe}(x,y,z)=\frac{1}{R_s}[x_{s,TEe}(x_0,y_0,z_0)x_0+y_{s,TEe}(x_0,y_0,z_0)y_0] \tag{42}$$

$$h_{p,TEe}(x,y,z) = -\frac{1}{R_s}\left[x_{p,TEe}(x_0,y_0,z_0)x_0 + y_{p,TEe}(x_0,y_0,z_0)y_0\right] \tag{43}$$

and x_{se}, y_{se}, ${\delta_e}^j$, and ${p_e}^j$ are the equilibrium positions of the shaft and pads, which are obtained from the static result of the CFD-solver (Part I). The thermal expansion displacements from the finite element analysis (FEA) solver in the static calculation are also included in Eqs. (42) and (43). The time derivative of the film thickness is also needed for the complete source terms for calculating the damping coefficients. The velocity perturbations $\Delta\dot{x}_{pb}$, $\Delta\dot{y}_{pb}$, $\Delta{\dot{\delta}_{pb}}^j$, and $\Delta{\dot{p}_{pb}}^j$ are substituted into $\dot{x}_{se}$, $\dot{y}_{se}$, ${\dot{\delta}_e}^j$, and ${\dot{p}_e}^j$, which appear in the time derivative of the film thickness Eq. (41) yielding

$$\frac{\partial h_e^j(x,\ y,\ z)}{\partial t} = -\frac{1}{R_s}\left[\{\Delta\dot{x}_{pb} - \Delta\dot{p}_{pb}\cos(\theta_p^j)\}x_0 + \{\Delta\dot{y}_{pb} - \Delta\dot{p}_{pb}\sin(\theta_p^j)\}y_0 + \Delta\dot{\delta}_{pb}R_s\{y_0\cos(\theta_p^j) - x_0\sin(\theta_p^j)\}\right] \tag{44}$$

Each velocity perturbation is substituted into the perturbed velocity source term of the transport equations, and the resultant pad moments and pad and journal reaction forces are utilized to calculate the full damping coefficient matrix as in Eq. (45). The components of the matrix are determined similarly with the calculation method of the stiffness coefficient.

$$\left[c_{brg}\right] = \left[\begin{array}{c:c} \mathbf{c}_{JJ} & \mathbf{c}_{JP} \\ \hdashline \mathbf{c}_{PJ} & \mathbf{c}_{PP} \end{array}\right] = \left[\begin{array}{c:c:c:c} c_{xx} & c_{xy} & \mathbf{c}_{x\delta} & \mathbf{c}_{xp} \\ \hdashline c_{yx} & c_{yy} & \mathbf{c}_{y\delta} & \mathbf{c}_{yp} \\ \hdashline \mathbf{c}_{\delta x} & \mathbf{c}_{\delta y} & \mathbf{c}_{\delta\delta} & \mathbf{c}_{\delta p} \\ \hdashline \mathbf{c}_{px} & \mathbf{c}_{\delta y} & \mathbf{c}_{p\delta} & \mathbf{c}_{pp} \end{array}\right] \tag{45}$$

2.3 Frequency Reduced Dynamic Coefficient and Log Decrement.

Industry practice, i.e., API 617 standard, requires reducing the large matrices of stiffness and damping coefficients in Eqs. (18) and (45) to 2 × 2 matrices relating x and y translations of the journal. This is somewhat driven by the preponderance of rotordynamics simulation codes that only accept the 2 × 2 matrices. The reduction is enabled by assuming the oscillation frequency of the pads and journal. The most common practice is to assume that the vibration frequency equals the spin frequency in which case the coefficients are referred to as synchronously reduced coefficients. The 2 × 2 matrix forms for the TPJB coefficient matrices are then used in rotordynamics codes to calculate stability, critical speed, imbalance response, etc., of the rotor system.

The original journal-pad dynamic equilibrium equation is

$$[m_{brg}][\ddot{q}] + [c_{brg}][\dot{q}] + [k_{brg}][q] = [F_{brg}] \tag{46}$$

where $[k_{brg}]$ and $[c_{brg}]$ are the full stiffness and damping coefficient matrices with 12 × 12 dimensions, respectively. The $[m_{brg}]$ is the mass matrix including the shaft-pad mass and moment of inertia.

$$[m_{brg}] = \begin{bmatrix} \mathbf{m}_{JJ} & 0 \\ 0 & \mathbf{m}_{PP} \end{bmatrix} \tag{47}$$

The subscript J denotes the shaft degrees-of-freedom and P indicates the pad degrees-of-freedom. The pads and journal are assumed to all vibrate with the common frequency ν, i.e.,

$$[q] = \begin{bmatrix} \mathbf{q}_J \\ \mathbf{q}_P \end{bmatrix} = e^{i\nu t}\begin{bmatrix} \bar{\mathbf{q}}_J \\ \bar{\mathbf{q}}_P \end{bmatrix} \tag{48}$$

which is typically selected as the spin frequency. In this case, the coefficients are said to be "synchronously reduced."

Substitution of Eq. (48) into Eq. (46) yields

$$\begin{bmatrix} \mathbf{Z}_{JJ} & \mathbf{Z}_{JP} \\ \mathbf{Z}_{PJ} & \mathbf{Z}_{PP} \end{bmatrix}\begin{bmatrix} \bar{\mathbf{q}}_J \\ \bar{\mathbf{q}}_P \end{bmatrix} = \begin{bmatrix} \bar{\mathbf{F}}_J \\ \mathbf{0} \end{bmatrix} + \nu^2\begin{bmatrix} \mathbf{M}_{JJ} & \mathbf{0} \\ \mathbf{0} & \mathbf{0} \end{bmatrix}\begin{bmatrix} \bar{\mathbf{q}}_J \\ \bar{\mathbf{q}}_P \end{bmatrix} \tag{49}$$

where

$$\mathbf{Z}'_{JJ} = \mathbf{Z}_{JJ} - \mathbf{Z}_{JP}{\mathbf{Z}_{PP}}^{-1}\mathbf{Z}_{PJ} \tag{50}$$

$$\mathbf{Z}_{JJ} = i\nu\mathbf{c}_{JJ} + \mathbf{k}_{JJ} \tag{51}$$

$$\mathbf{Z}_{JP} = i\nu\mathbf{c}_{JP} + \mathbf{k}_{JP} \tag{52}$$

$$\mathbf{Z}_{PJ} = i\nu\mathbf{c}_{PJ} + \mathbf{k}_{PJ} \tag{53}$$

$$\mathbf{Z}_{PP} = i\nu\mathbf{c}_{PP} + \mathbf{k}_{PP} - \nu^2\mathbf{m}_{PP} \tag{54}$$

The bottom row of Eq. (49) is substituted into the top row to obtain

$$-\nu^2\mathbf{m}_{JJ}\bar{\mathbf{q}}_J + \mathbf{Z}'_{JJ}\bar{\mathbf{q}}_J = \bar{\mathbf{F}}_J \tag{55}$$

Substitution of Eq. (50) yields the journal motion equation

$$-\nu^2\mathbf{m}_{JJ}\bar{\mathbf{q}}_J + i\nu\hat{\mathbf{c}}_{JJ}\bar{\mathbf{q}}_J + \hat{\mathbf{k}}_{JJ}\bar{\mathbf{q}}_J = \bar{\mathbf{F}}_J \tag{56}$$

By comparing Eq. (55) to Eq. (56), the final synchronously reduced dynamic coefficients can be written as in Eqs. (57) and (58).

$$\hat{\mathbf{k}}_{JJ} = \mathrm{real}(\mathbf{Z}'_{JJ}) \tag{57}$$

$$\hat{\mathbf{c}}_{JJ} = \frac{1}{\nu}\,\mathrm{imag}(\mathbf{Z}'_{JJ}) \tag{58}$$

Bearing performance is often characterized by determining the log dec of a rigid (Jeffcott) rotor supported symmetrically on two identical bearings. If λ_i is an eigenvalue of the Jeffcott rotor, the log decrement is defined as

$$\delta_{dec,i} = \frac{2\pi\xi_i}{\sqrt{1-\xi_i^2}} \tag{59}$$

$$\xi_i = \frac{\mathrm{real}(\lambda_i)}{|\lambda_i|} \tag{60}$$

2.4 Calculation Procedure.

Calculation of the dynamic coefficients is performed with a CFD-solver and a dedicated MATLAB code. For the sake of simplicity, the effects of pad deflections resulting from the perturbations are ignored, eliminating the need for the FEA deflection solver employed in Part I. Thermal and centrifugal force deformations of the pads and shaft are loaded at the initial stage to include these effects for establishing static equilibrium film thickness expressions about which perturbations occur.

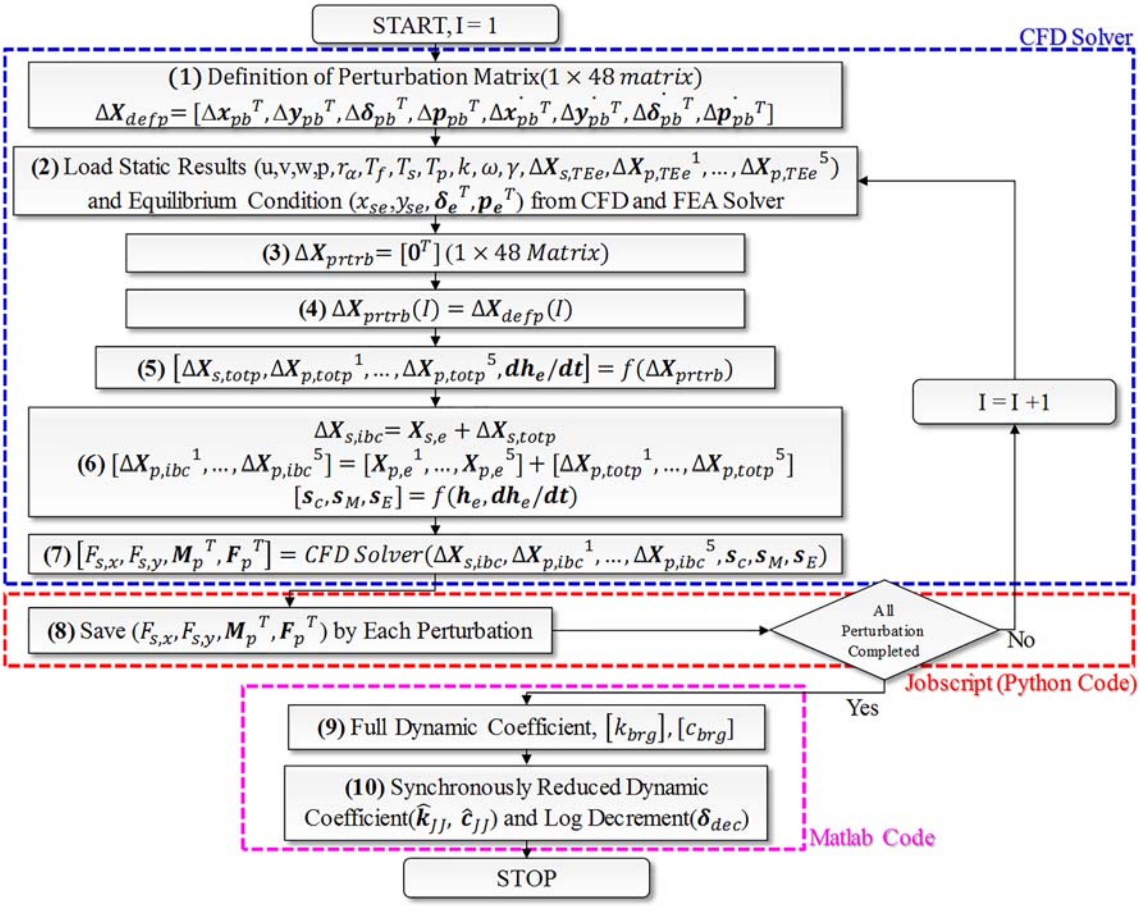

Fig. 5 Calculation procedure for obtaining frequency reduced, TPJB stiffness, and damping coefficients

Figure 5 provides a flow diagram of the overall calculation procedure for obtaining the TPJB stiffness and damping coefficients. The following is a further explanation of the diagram:

(1) All displacement ($\Delta\boldsymbol{x}_{pb}{}^T$, $\Delta\boldsymbol{y}_{pb}{}^T$, $\Delta\boldsymbol{\delta}_{pb}{}^T$, $\Delta\boldsymbol{p}_{pb}{}^T$) and velocity perturbations ($\Delta\dot{\boldsymbol{x}}_{pb}{}^T$, $\Delta\dot{\boldsymbol{y}}_{pb}{}^T$, $\Delta\dot{\boldsymbol{\delta}}_{pb}{}^T$, $\Delta\dot{\boldsymbol{p}}_{pb}{}^T$), including transitional and angular motions, are defined in the 1 × 24 perturbation definition matrix.

(2) All of the CFD model-dependent variables (u, v, w, p, r_α, T_f, T_s, T_p, k, ω, γ) from the static equilibrium solution (Part I) are imported as the initial values in order to accelerate the convergence for each perturbation simulation. Likewise, the thermal and centrifugal induced displacements of the pads, pivots, and journal ($\Delta\boldsymbol{X}_{s,TEe}$, $\Delta\boldsymbol{X}_{p,TEe}{}^1, \dots, \Delta\boldsymbol{X}_{p,TEe}{}^5$) are imported from the FEA-solver's static equilibrium solution. The equilibrium positions (x_{se}, y_{se}, $\boldsymbol{\delta}_e{}^T$, $\boldsymbol{p}_e{}^T$) are loaded from the CFD-solver in order to apply them to the film thickness model of the perturbed velocity source terms for calculating damping coefficients.

(3–4) The perturbation matrix $\Delta\boldsymbol{X}_{prtrb}$ is updated with the perturbation on the current degree of freedom.

(5) The perturbation matrix $\Delta\boldsymbol{X}_{prtrb}$ is substituted into the total perturbation displacement equations of the shaft and pad, and the time derivative equation of the film thickness.

(6) The shaft $\Delta\boldsymbol{X}_{s,totp}$ and pad total perturbation displacement vectors $[\Delta\boldsymbol{X}_{p,totp}{}^1, \dots, \Delta\boldsymbol{X}_{p,totp}{}^5]$ are added with the shaft total displacements $\boldsymbol{X}_{s,e}$ and the pad total displacements $[\Delta\boldsymbol{X}_{p,e}{}^1, \dots, \Delta\boldsymbol{X}_{p,e}{}^5]$ from the static equilibrium position simulation. The summed displacements are imposed at the interface boundaries $\Delta\boldsymbol{X}_{s,ibc}$, $\Delta\boldsymbol{X}_{p,ibc}{}^1, \dots, \Delta\boldsymbol{X}_{p,ibc}{}^5$ between the shaft-pad and fluid film for calculating the stiffness coefficient matrix. The equilibrium condition film thickness matrix $\boldsymbol{h}_e$, and the time derivative of the film thickness matrix $\boldsymbol{dh}_e/\boldsymbol{dt}$ for velocity perturbations are substituted into the continuity, momentum, and energy equations as source terms [$\boldsymbol{s}_C$, $\boldsymbol{s}_M$, $\boldsymbol{s}_E$]. The resulting pressure and force results are then utilized for calculating the damping coefficients.

(7) The prescribed displacement at the interface boundaries $\Delta\boldsymbol{X}_{s,ibc}$, $\Delta\boldsymbol{X}_{p,ibc}{}^1, \dots, \Delta\boldsymbol{X}_{p,ibc}{}^5$ and the source terms [$\boldsymbol{s}_C$, $\boldsymbol{s}_M$, $\boldsymbol{s}_E$] in the subdomains are applied in the CFD-solver for each perturbation. The resulting forces $F_{s,x}$, $F_{s,y}$, and $\boldsymbol{F}_p{}^T$ acting on the shaft and pads and moment $\boldsymbol{M}_p{}^T$ are then calculated.

(8) The reaction forces on the shaft and pads $F_{s,x}$, $F_{s,y}$, and $\boldsymbol{F}_p{}^T$ and pad moments $\boldsymbol{M}_p{}^T$ are stored for each perturbation, and steps (2)–(8) are repeated for all perturbations.

(9–10) The stored $F_{s,x}$, $F_{s,y}$, $\boldsymbol{F}_p{}^T$, and $\boldsymbol{M}_p{}^T$ are transferred to the MATLAB code in which the full dynamic coefficient matrices $[k_{brg}]$ and $[c_{brg}]$, synchronously reduced dynamic coefficient matrices $\hat{\mathbf{k}}_{JJ}$ and $\hat{\mathbf{c}}_{JJ}$, and log decrements $\boldsymbol{\delta}_{dec}$ are calculated.

3 Description of Reynolds Model for Calculation of Dynamic Coefficient

As in the static case in Part I, a Reynolds solution is utilized to benchmark the CFD results for the idealized without mixing effect case. The dynamic coefficients from the Reynolds model are calculated in a manner similar to the CFD model. The Reynolds static equilibrium results in Part I are utilized to form the reference state about which the perturbations are taken to determine the dynamic coefficients. In addition, the input parameters including operating condition and rotor-bearing system dimension are given in Part I. The perturbations cause changes in the film thickness distributions that are utilized in the Reynolds model. Reaction forces and moments are determined by integrating the predicted pressure distributions resulting from the perturbations. The reaction forces on the shaft and pads and moments on the pads are utilized to calculate the stiffness coefficients. Velocity perturbations are substituted into the film thickness time derivative term in the Reynolds equation to calculate the damping coefficients. The major difference between the CFD and Reynolds model is the governing equations for the fluid film domain. The Reynolds model is derived by neglecting the inertia effect from the transient term in the momentum equation, the radial pressure distribution through the film thickness, and the shaft curvature effect. Thus the transient term $\partial \rho_f u_i / \partial t$ and convective term $\partial \rho_f u_i u_j / \partial x_j$ of the momentum equation for the perturbations are ignored in the Reynolds model, where the convective term causes the fluid inertia effect. The transient term $\partial \rho_f C_{p,f} T_f / \partial t$ in the energy equation is also neglected for the perturbation calculations. Thus, it is assumed that the temperature distribution remains at its static equilibrium state as calculated in Part I, for all perturbations. This saves a significant amount of computer time. It is a reasonable assumption to neglect the transient term of the energy equation and transient and convective terms of the momentum equation due to their small influences for very small perturbations.

The static results in Part I showed a high sensitivity to the MC in the Reynolds model. This resulted since the MC of the Reynolds model is an oversimplified approach to account for the complex flow field occurring between the pads BP and in the pad entrances. The following sections illustrate the effects that varying the mixing MC has on the dynamic coefficients and includes comparisons with the CFD results.

4 Dynamic Performance Results

4.1 Computational Fluid Dynamics—Reynolds Comparison for the "Without Mixing Effect" Condition. Simulations results are presented for the "with mixing effect" and "without mixing effect" conditions. The "with mixing effect" condition means that the CFD and Reynolds models consider the between pad BP regions, the former including detailed fluidic and thermal models of the complex flow that occurs BP, and the latter utilizing an approximate MC to establish pad inlet flow temperatures by considering makeup and carryover flows. The "without mixing effect" condition neglects consideration of the flow and thermal conditions present BP and instead represents an idealized condition where pad inlet flow temperatures are uniform along the pad length and identical in both the CFD and Reynolds models. This provides a validation check of the CFD model that would be expected to closely agree with the Reynolds model for the assumed idealized boundary conditions. Part I provides the detailed descriptions of these two models. As in Part I, three cases are considered for comparing the CFD and Reynolds models results: ***(A)*** *rigid pivots and no thermal deformations,* ***(B)*** *flexible pivots, and* ***(C)*** *flexible pivots and thermal deformations.* This section presents simulation results for the "without mixing effect" models and Sec. 4.2 provides simulation results for the "with mixing effect" models. Figures 6–8 present nondimensional stiffness, damping and log decrement versus speed comparisons, including results from Reynolds models with both 2D and 3D thermal solutions and from the CFD model.

The nondimensional stiffness (K_{ij}) and damping (C_{ij}) coefficients are defined in terms of their dimensional counterparts ($\hat{k}_{ij}$, $\hat{c}_{ij}$) by

$$K_{ij} = \frac{C_{l,p} \hat{k}_{ij}}{W}, \quad C_{ij} = \frac{C_{l,p} \omega_s \hat{c}_{ij}}{W}$$

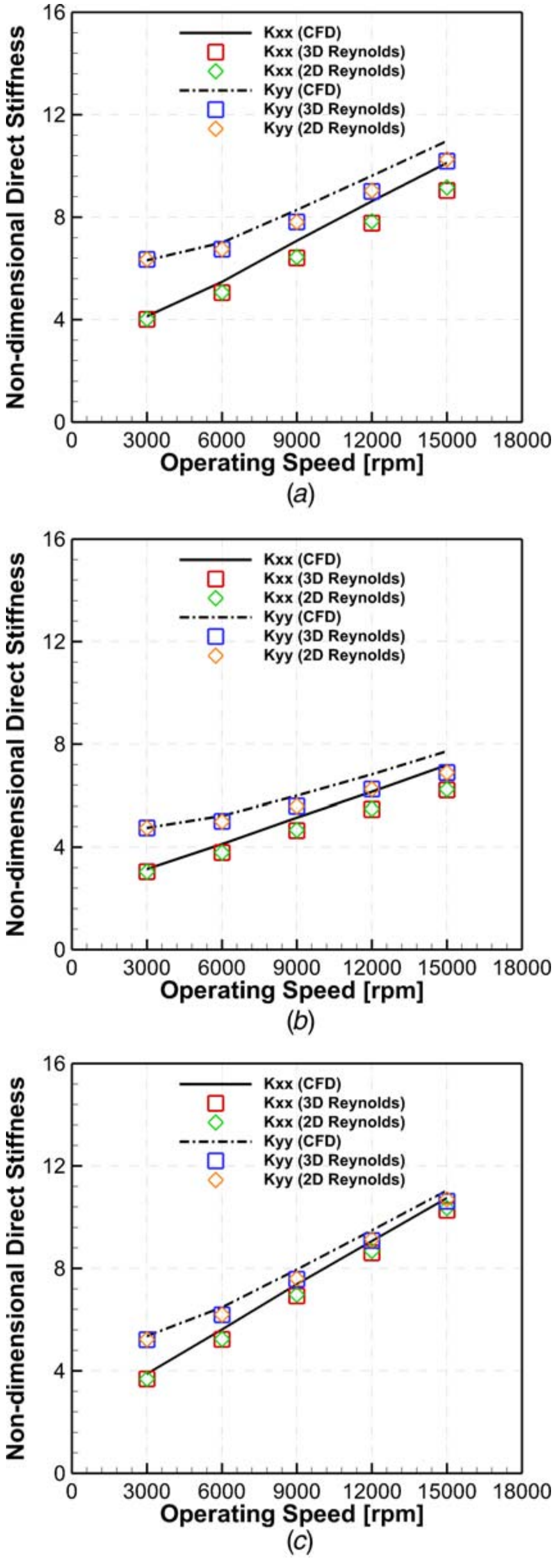

Fig. 6 Nondimensional direct stiffness of "without mixing effect" model: (*a*) case A, (*b*) case B, and (*c*) case C effects

The rotor mass utilized in the Jeffcott rotor model for determining log decrements is 1019 kg. The x and y log decrements are slightly different as shown in Fig. 8 and result from the TPJB having different stiffness and damping in the x and y directions.

The Reynolds models are indicated by symbols and the CFD results by solid lines on the plots. The results confirm a closed agreement between the CFD and Reynolds models results for the idealized "without mixing effect" study. This is true for the conditions represented by all cases: (A), (B), and (C).

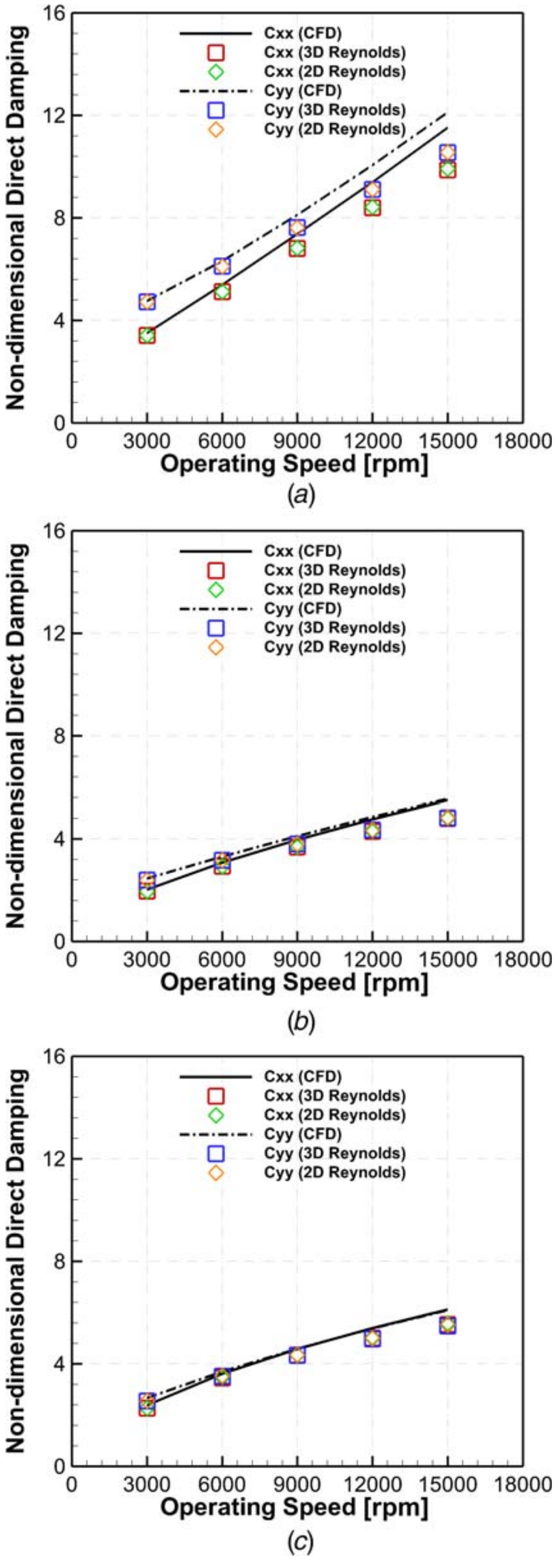

(*a*)

(*b*)

(*c*)

Fig. 7 Nondimensional direct damping of "without mixing effect" model: (*a*) case A, (*b*) case B, and (*c*) case C effects

The discrepancies between the Reynolds and CFD models are relatively small and most likely due to the simplifying assumptions employed in the Reynolds model, including neglect of the transient term $\partial\rho_f u_i/\partial t$ and convective terms $\partial\rho_f u_i u_j/\partial x_j$ in the momentum equation and the transient term $\partial\rho_f C_{p,f} T_f/\partial t$ in the energy equation. The neglect of the convective and transient terms is confirmed to be reasonable assumptions in the Reynolds model, based on the discrepancies with the CFD results only being minor.

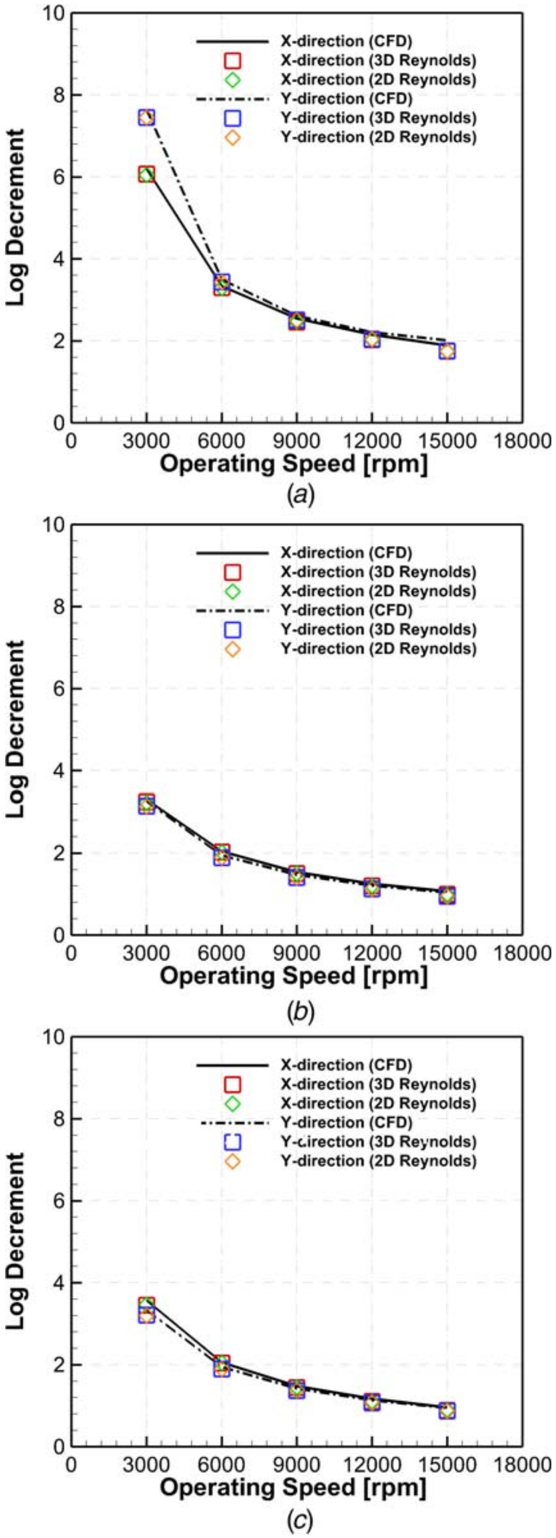

(*a*)

(*b*)

(*c*)

Fig. 8 Log decrement of "without mixing effect" model: (*a*) case A, (*b*) case B, and (*c*) case C effects

The following conclusions are based on the "without mixing effect" model: (1) the CFD and Reynolds model results agree very well supporting the accuracy of the CFD model for modeling pad flows, (2) the nondimensional stiffness and damping coefficients increase monotonically with speed, (3) in contrast the log decrement monotonically decreases with speed, (4) the nondimensional direct stiffness and damping coefficients and the log decrement decrease significantly for the with pivot flexibility case (B), relative to the rigid pivot case (A), and (5) the nondimensional direct stiffness and damping coefficients increase significantly for the with pivot flexibility and thermal expansion case (C), relative to the flexible pivot case (B).

4.2 Computational Fluid Dynamics—Reynolds Comparison for the "With Mixing Effect" Condition. The "with mixing effect" condition means that the CFD and Reynolds models consider the between pad BP regions, the former including detailed fluidic and thermal models of the complex flow that occurs BP, and the latter utilizing an approximate MC to establish pad inlet flow temperatures by considering makeup and carryover flows. The Reynolds model has been widely used for the prediction of TPJB stiffness and damping coefficients [1–8] due to its relatively low computational time, presence in software regularly used in industry and its validation with a limited number of experiments. Part I showed that the predicted static response results for TPJB could vary widely as the MC changes and deviate significantly from the more sophisticated CFD model results. The MC is a model parameter that is left to the analyst to select based on limited experience. In comparison, the CFD model that includes the complex flow and thermal states between pads can remove the inaccuracy and uncertainty of the MC approach. The following figures and discussion compare the "Reynolds + MC" model with the CFD model dynamic coefficients and log decrements, considering the cases: *(**A**) rigid pivots and no thermal deformations, (**B**) flexible pivots, and (**C**) flexible pivots and thermal deformations*.

Figure 9(*a*) corresponds to case A and shows a high sensitivity of direct stiffness (K_{xx}) to the Reynolds model's MC and that the CFD K_{xx} are near the low MC Reynolds K_{xx} at low operating speeds (<9000 rpm), and near the high MC Reynolds K_{xx} at higher operating speeds (>9000 rpm). Figure 9(*b*) corresponds to case B and shows a medium sensitivity of direct stiffness (K_{xx}) to the Reynolds model's MC and that the CFD K_{xx} are near the low MC Reynolds K_{xx} at all operating speeds. Figure 9(*c*) corresponds to case C and shows a high sensitivity of direct stiffness (K_{xx}) to the Reynolds model's MC, and that the CFD K_{xx} are out of the range of values bracketed by the low and high MC Reynolds models. The discrepancy between the Reynolds and CFD models increases with increasing speed and attains a maximum value of 68.0%.

Figure 10(*a*) corresponds to case A and shows a medium sensitivity of direct stiffness (K_{yy}) to the Reynolds model's MC and that the CFD K_{yy} are near the high MC Reynolds K_{yy} at all operating speeds. Figure 10(*b*) corresponds to case B and shows a small sensitivity of direct stiffness (K_{yy}) to the Reynolds model's MC and that the CFD K_{yy} are near the low MC Reynolds K_{yy} at all operating speeds. Figure 10(*c*) corresponds to case C and shows a high sensitivity of direct stiffness (K_{yy}) to the Reynolds model's MC and that the CFD K_{yy} are out of the range of values bracketed by the low and high MC Reynolds models. The discrepancy between the Reynolds and CFD models increases with increasing speed and attains a maximum value of 63.6%.

Figures 11 and 12 show the cross-coupled stiffness coefficients (K_{xy}, K_{yx}), respectively, versus operating speed. Both cross-coupled stiffness coefficients (K_{xy}, K_{yx}) are nearly zero in the case of no thermal expansion and increase in magnitude as the operating speed increases.

Figure 13(*a*) corresponds to case A and shows a high sensitivity of direct damping (C_{xx}) to the Reynolds model's MC and that the CFD C_{xx} are near the low MC Reynolds C_{xx} at all operating speeds. Figure 13(*b*) corresponds to case B and shows a medium sensitivity of direct damping (C_{xx}) to the Reynolds model's MC and that the CFD C_{xx} are near the low MC Reynolds C_{xx} at all operating speeds. Figure 13(*c*) corresponds to case C and shows a low sensitivity of direct damping (C_{xx}) to the Reynolds model's MC and that the CFD C_{xx} are out of the range of values bracketed by the low and high MC Reynolds models. The discrepancy between the Reynolds and CFD models increases with increasing speed and attains a maximum value of 53.5%.

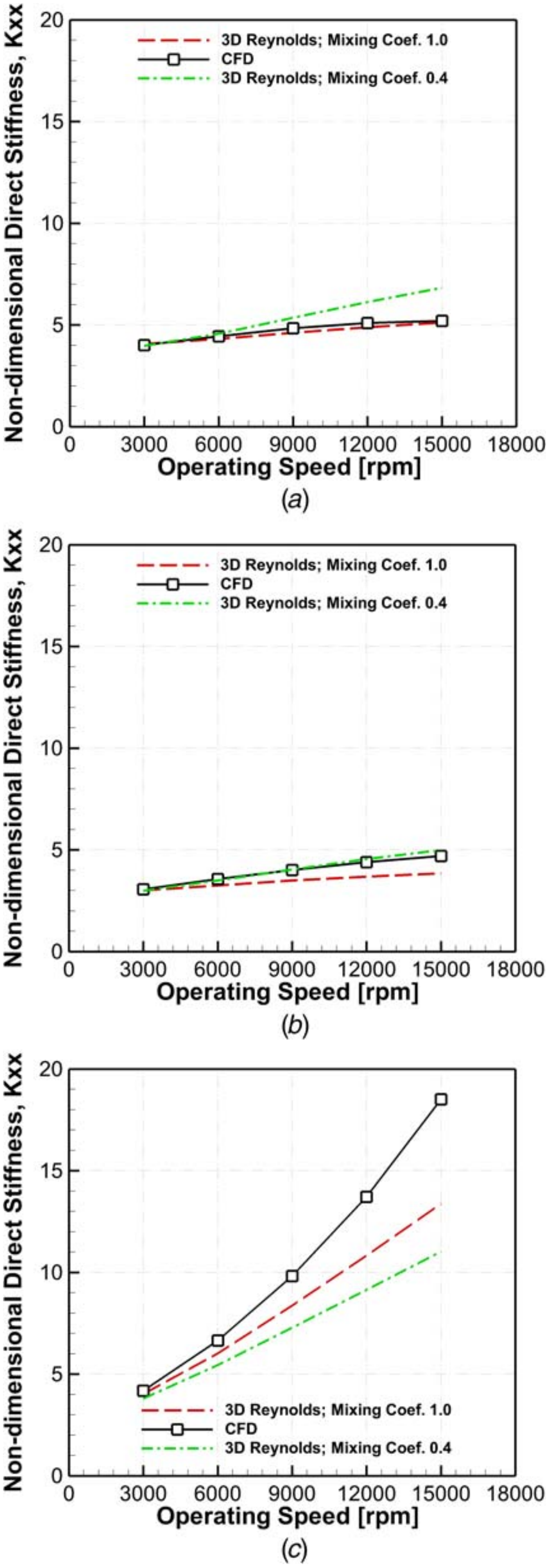

Fig. 9 Nondimensional direct stiffness (K_{xx}) of the "with mixing effect" model for (*a*) case A, (*b*) case B, and (*c*) case C

Figure 14(*a*) corresponds to case A and shows a high sensitivity of direct damping (C_{yy}) to the Reynolds model's MC and that the CFD C_{yy} are near the low MC Reynolds C_{yy} at all operating speeds. Figure 14(*b*) corresponds to case B and shows a medium sensitivity of direct damping (C_{yy}) to the Reynolds model's MC and that the CFD C_{yy} are near the low MC Reynolds C_{yy} at all

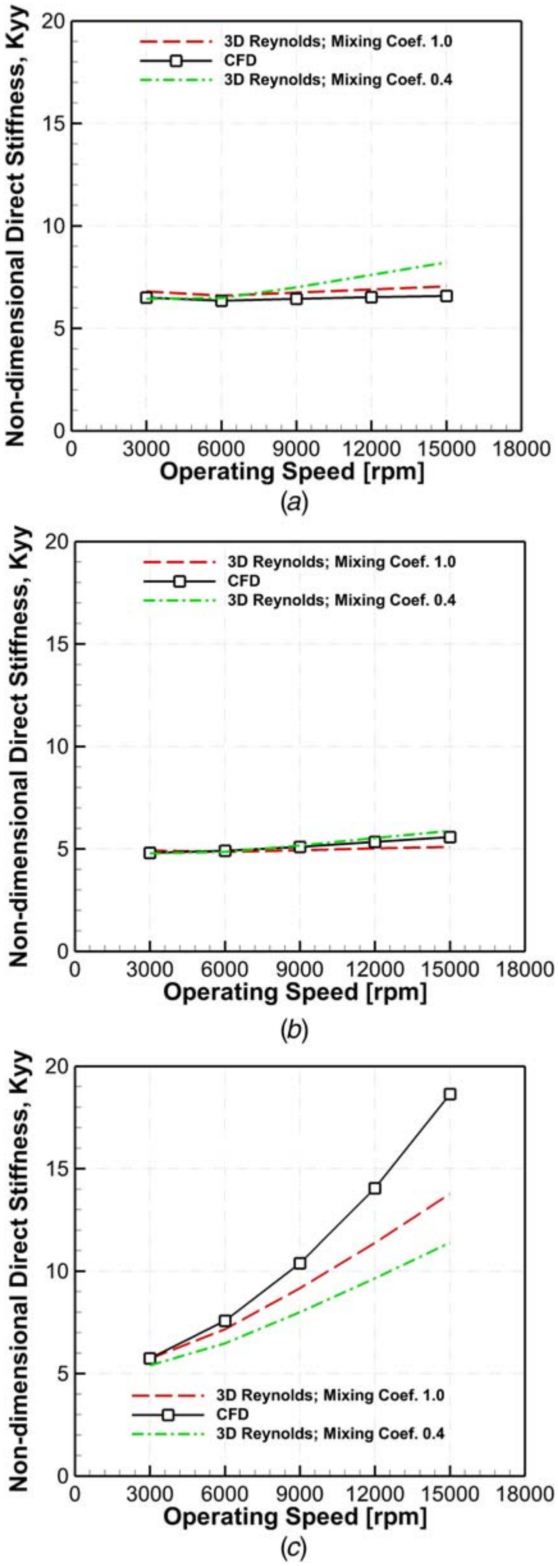

Fig. 10 Nondimensional direct stiffness (K_{yy}) of the "with mixing effect" model for (a) case A, (b) case B, and (c) case C

operating speeds. Figure 14(*c*) corresponds to case C and shows a low sensitivity of direct damping (C_{yy}) to the Reynolds model's MC and that the CFD C_{yy} are out of the range of values bracketed by the low and high MC Reynolds models. The discrepancy between the Reynolds and CFD models increases with increasing speed and attains a maximum value of 48.1%.

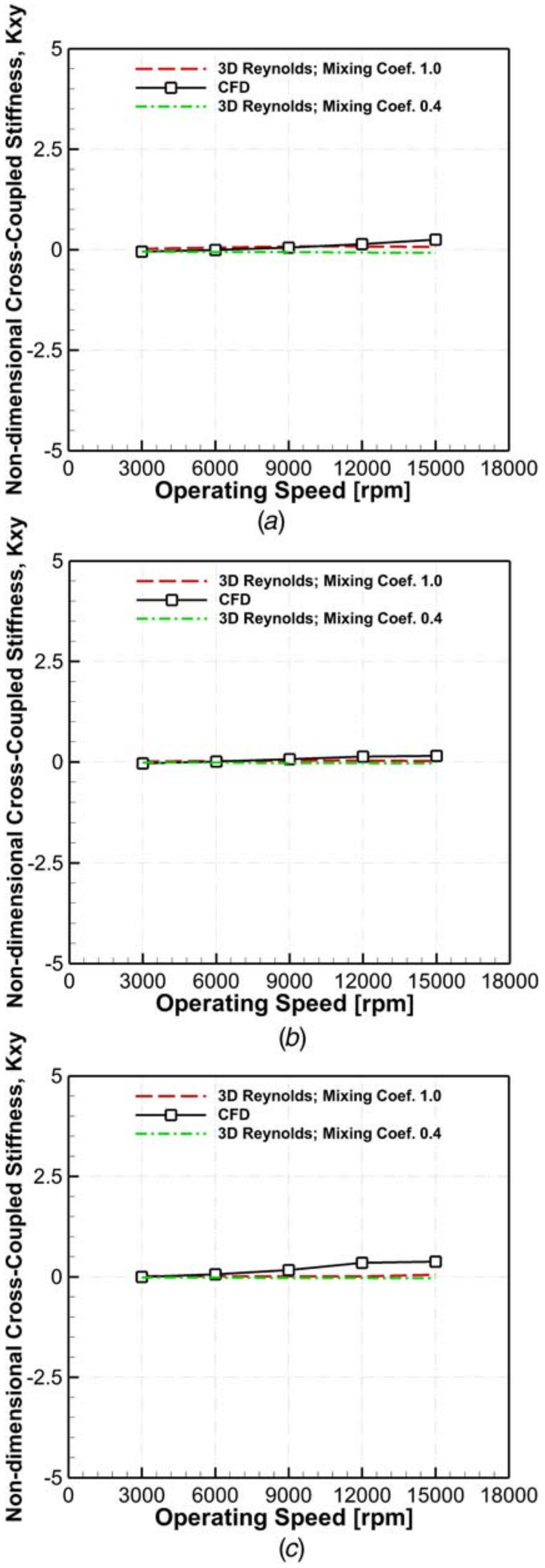

Fig. 11 Nondimensional cross-coupled stiffness (K_{xy}) of the "with mixing effect" model for (a) case A, (b) case B, and (c) case C

Figures 15 and 16 show the cross-coupled damping coefficients (C_{xy}, C_{yx}) versus speed. The values remain near zero for cases A and B, but for case C, CFD is predicted to attain a level that might significantly aid in stabilizing a rotor system. This is a

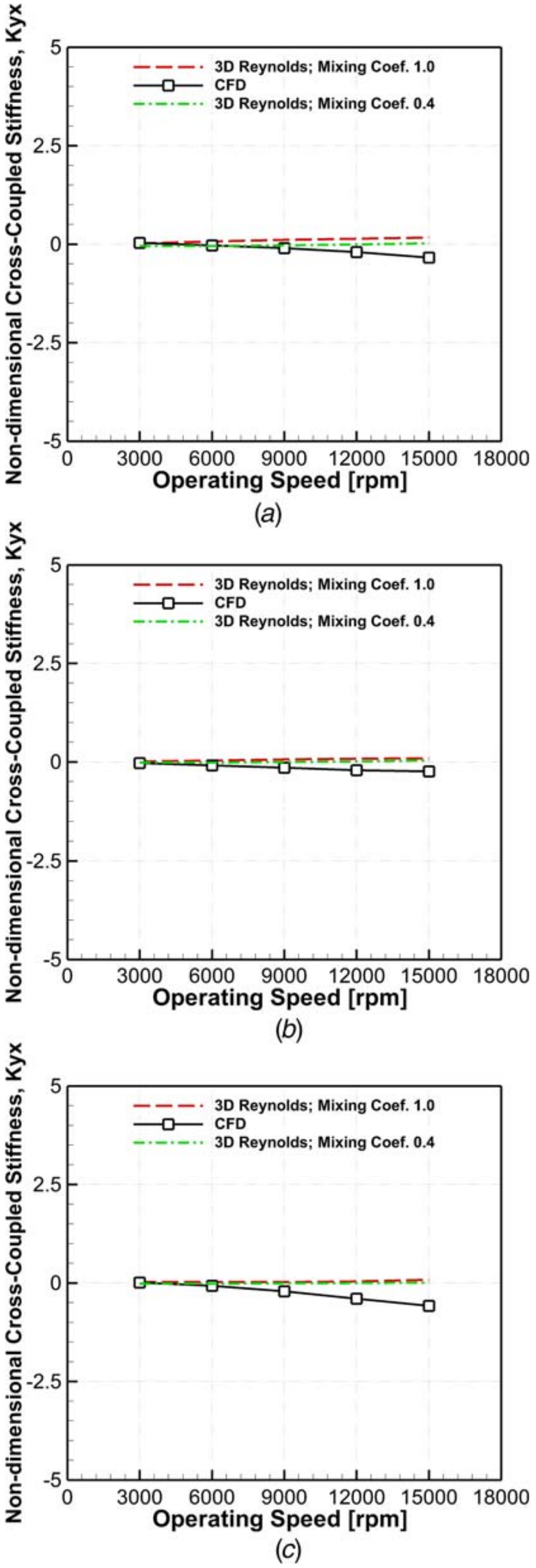

(*a*)

(*b*)

(*c*)

Fig. 12 Nondimensional cross-coupled stiffness (K_{yx}) of the "with mixing effect" model for (*a*) case A, (*b*) case B, and (*c*) case C

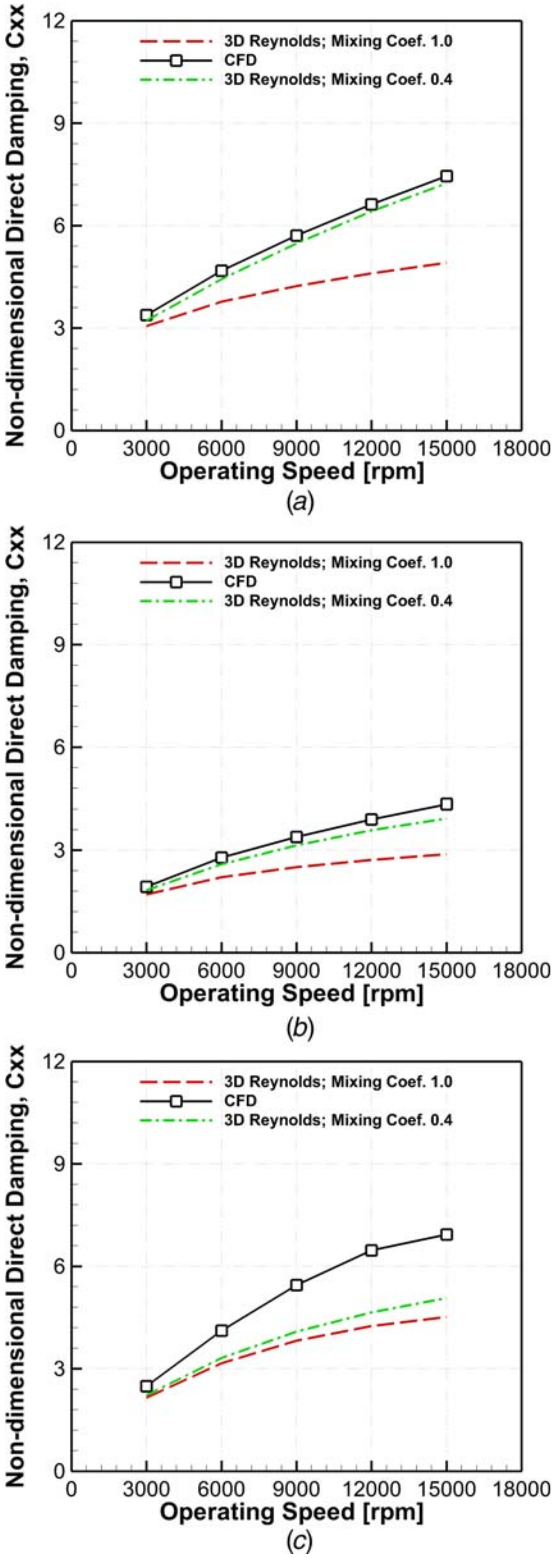

(*a*)

(*b*)

(*c*)

Fig. 13 Nondimensional direct damping (C_{xx}) of the "with mixing effect" model for (*a*) case A, (*b*) case B, and (*c*) case C

marked deviation from the Reynolds-MC model predictions that stay near zero in case C.

The Reynolds model assumes a uniform film temperature in the radial and axial direction at the pad inlet. However, there actually exists a spatially varying film temperature distribution at the pad inlet. The Reynolds zero radial temperature gradient assumption at the pad inlet reduces the heating of the shaft by the film near the pad inlet. This causes a significant difference in the shaft temperature predictions by the Reynolds and CFD methods. This in turn causes a thinner film in the CFD model, which also causes a deviation between the CFD and Reynolds dynamic coefficients. The better description is presented in Part I, including plots of heat flux and

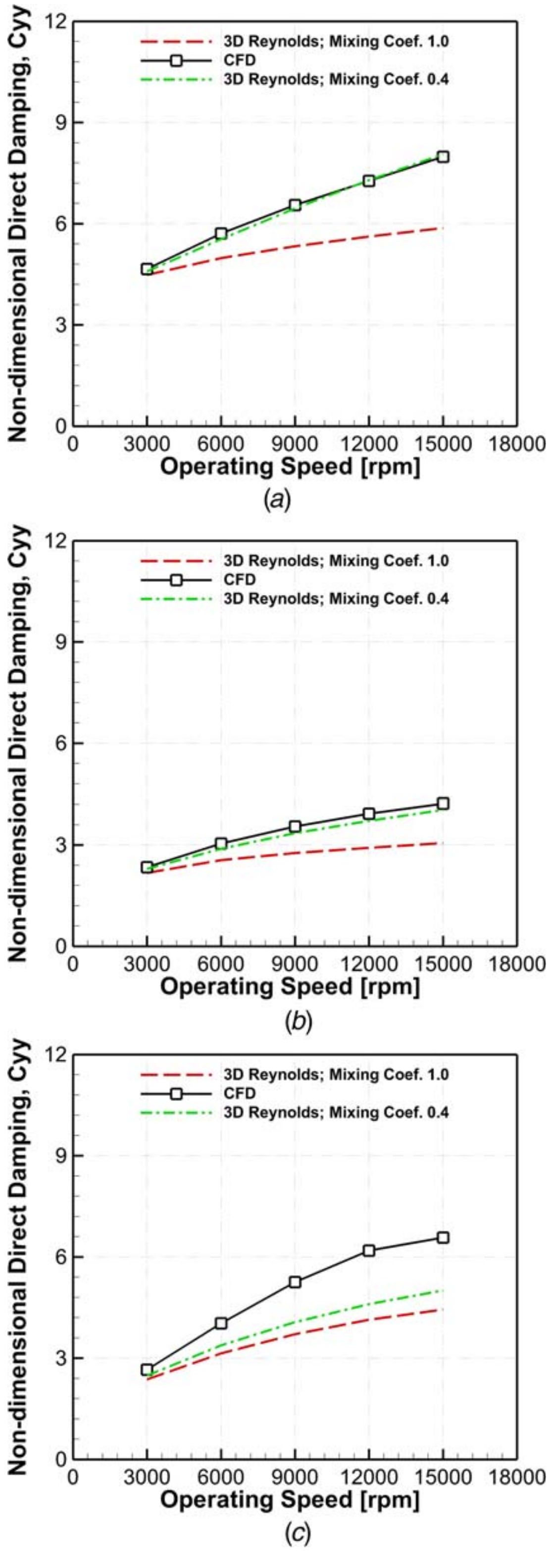

Fig. 14 Nondimensional direct damping (C_{yy}) of the "with mixing effect" model for (*a*) case A, (*b*) case B, and (*c*) case C

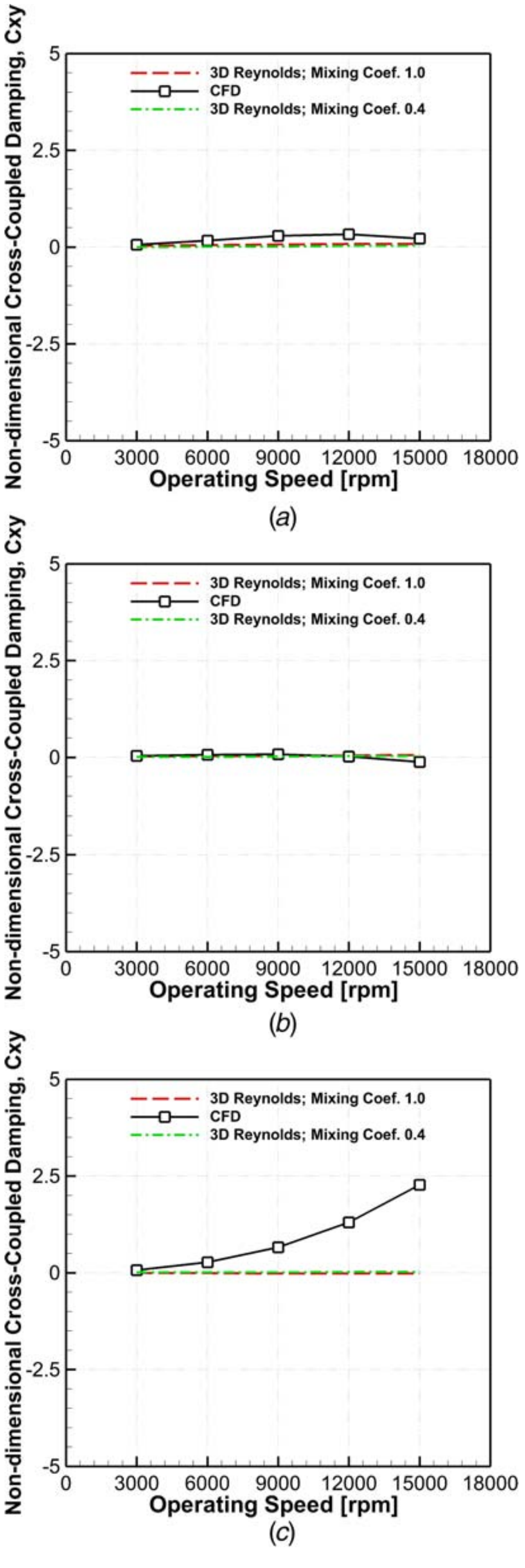

Fig. 15 Nondimensional cross-coupled damping (C_{xy}) of the "with mixing effect" model for (*a*) case A, (*b*) case B, and (*c*) case C

temperature distribution at the shaft surface. The key point is that the Reynolds film temperature assumption is overly simplistic and leads to large discrepancies compared with the CFD model.

Figures 17 and 18 show x and y mode log decrements versus speed, considering CFD and Reynolds predictions for cases A, B, and C. The log decrements are obtained from the eigenvalues of a Jeffcott rotor of mass 1019 kg, supported symmetrically with two identical TPJB, as given in Eqs. (53) and (54). Modal stability increases with log decrement and is unstable for negative log decrement values. The results show low sensitivity to MC with the Reynolds model and generally slightly higher values for the CFD model, compared with the Reynolds-MC model. Although the

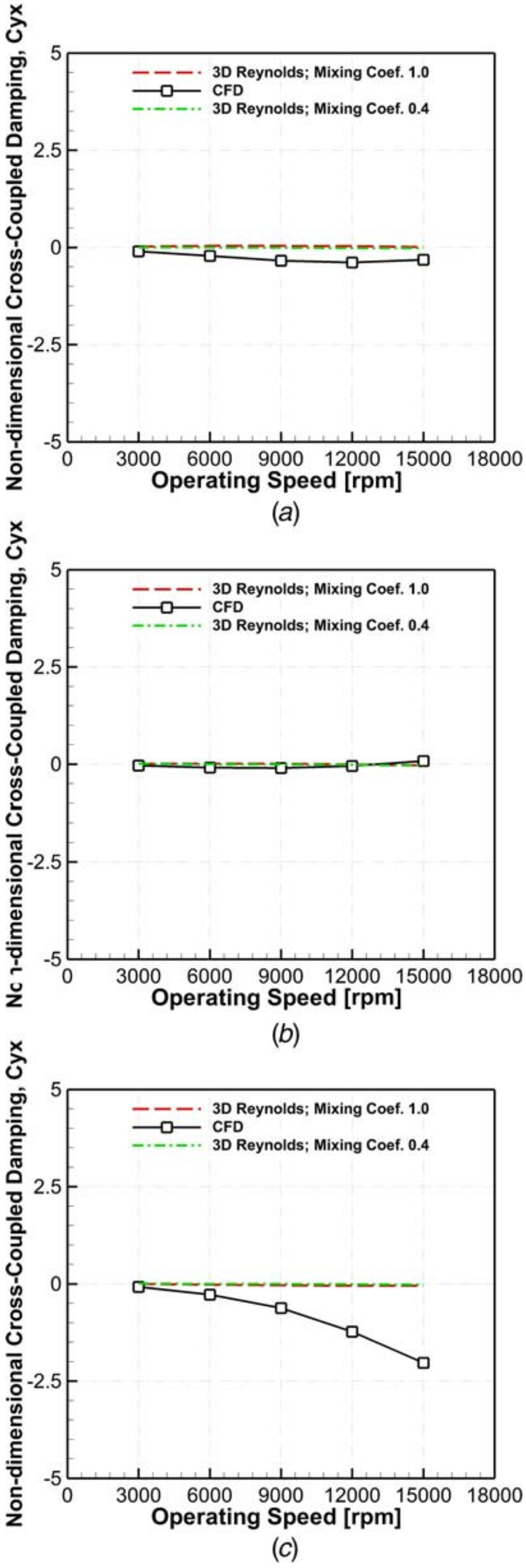

Fig. 16 Nondimensional cross-coupled damping (C_{yx}) of the "with mixing effect" model for (*a*) case A, (*b*) case B, and (*c*) case C

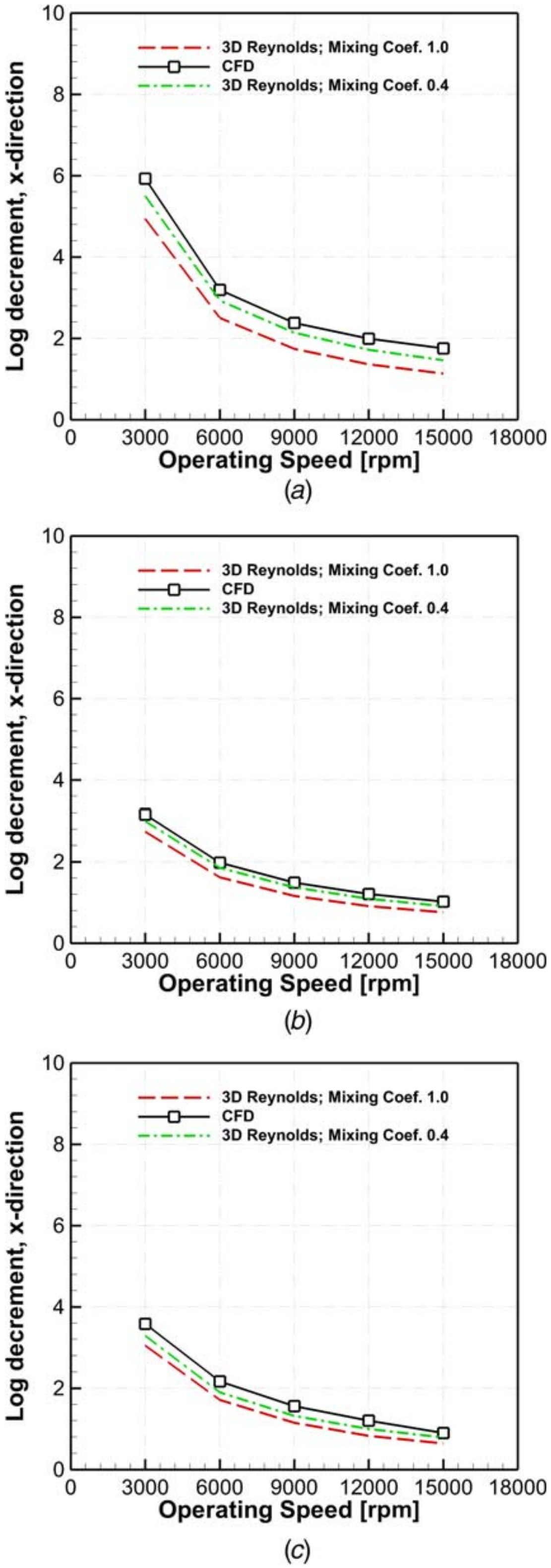

Fig. 17 Log decrement (*x*-direction) of the "with mixing effect" model for (*a*) case A, (*b*) case B, and (*c*) case C

CFD and Reynolds predicted log decrements are quite similar, this result corresponds only to a simple Jeffcott rotor model and should not be assumed to apply for more complex rotor systems. Figures 17 and 18 also show that log decrements can decrease considerably when the model includes pivot flexibility.

5 Conclusions

This paper compares the conventional Reynolds model of a TPJB to a new CFD-FSI model for calculation of stiffness and damping coefficients and log decrements of Jeffcott rotor supported by the TPJB. The Reynolds model along with the accompanying thin-film

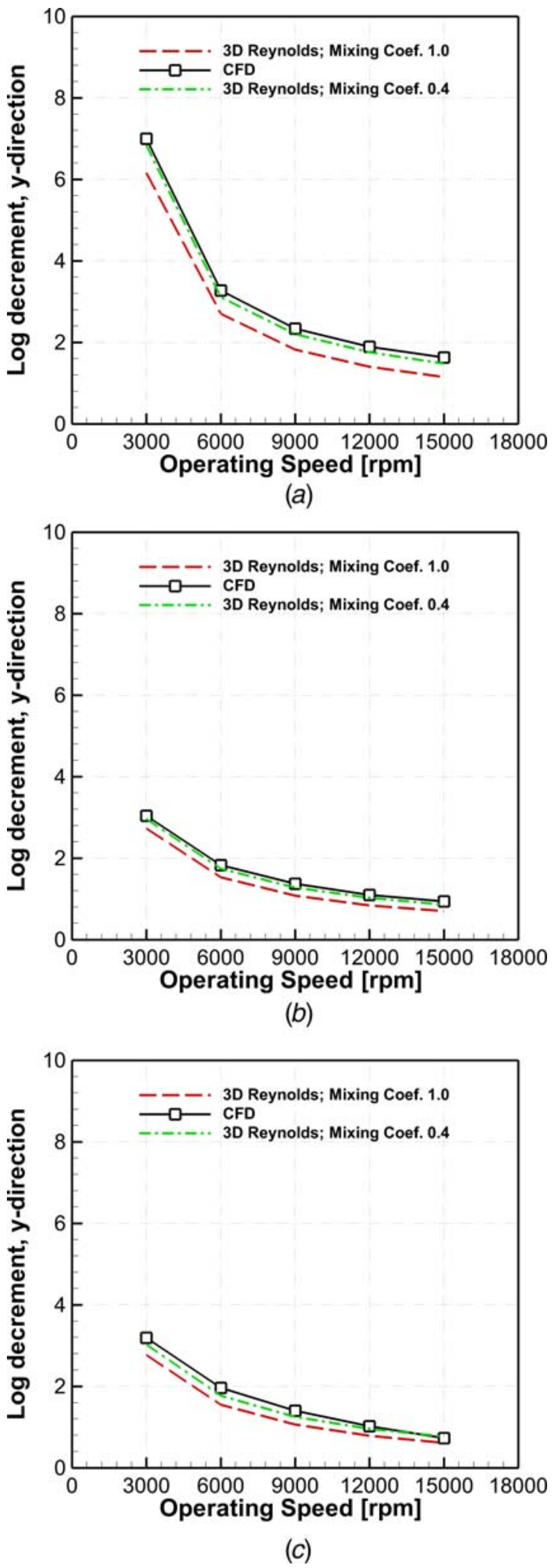

Fig. 18 Log decrement (y-direction) of the "with mixing effect" model for (*a*) case A, (*b*) case B, and (*c*) case C

energy equation has provided excellent tools for predicting thin-film pressures and temperatures in many areas of engineering. This has been true as long as external and internal (dams, reliefs, etc.) boundary conditions are specified accurately and in regions where a full film exists. The Reynolds model relies on a zero-dimensional mixing theory for the complex flow and heat transfer which occurs BP to provide a uniform inlet temperature boundary condition at pad inlets. This is obviously very simplistic when compared with the 3D thermal–fluid model employed by CFD in solving the full Navier–Stokes and full energy equations BP. CFD has matured to a point of being generally viewed as reliable and robust. The improved accuracy provided by CFD for BP modeling will also improve the accuracy of all ensuing predictions due to the highly coupled, thermal–fluid–solid nature of the TPJB. In other words, the CFD model provides more accuracy, especially in its treatment of the complex flow and thermal states existing between pads BP where cooler supply oil is injected and mixed with hot oil carryover. The Reynolds model incorporates a MC to approximate the pad inlet temperatures; however, this approach is shown to be overly simplistic relative to CFD and has an inherent uncertainty in the lack of reliable guidelines for selecting the MC. The CFD-FSI approach presented is the first to include the solution of the 3D Navier–Stokes equation for calculating the dynamic coefficients of a TPJB. This approach includes the effects of 3D incompressible multiphase flow, thermal–fluid, transitional turbulence flow, thermal rotational shaft and pad motions, and thermal deformation effect. The results include TPJB stiffness and damping coefficients in full matrix and frequency (synchronous) reduced forms. Calculation of the stiffness and damping coefficients requires the initial static solution presented in Part I followed by the perturbation solutions described here in Part II. Detailed procedures were presented for prescribing perturbed displacements at the interface boundaries for calculating stiffness coefficients, and for including perturbed velocity source terms in the transport equations for calculating the damping coefficients.

The results of the "without mixing effect" simulations, which ignored the BP flows, provided an initial confirmation of the validity of the CFD approach, in terms of the close agreement of the stiffness and damping coefficients and log decrements, with the Reynolds based predictions. The "with mixing effect" cases included the BP regions in the CFD model and mixing coefficients in the Reynolds model. The aim of both of these approaches is to determine accurate temperature distributions at the pad inlets, with the CFD approach providing a highly detailed and accurate distribution and the Reynolds approach providing a bulk temperature approximation. The results showed that the stiffness and damping coefficients may be highly sensitive to the MC value used in the Reynolds model. Furthermore, the CFD predictions may be close to the low (0.4) MC value results, close to the high (1.0) MC value results, or even lie far outside of the results bracketed by the low and high MC values, when considering an entire operating speed range (0–15,000 rpm).

In the "without mixing effect," the close agreement between the methods shown in Fig. 6 is consistent with applying the same (yet artificial) boundary conditions in both methods. Meanwhile, the disparity between the CFD and Reynolds predicted dynamic coefficients increase significantly when thermal expansion effects are included (case C). This appears to result from the same trend in the static equilibrium solutions presented in Part I. The film thickness distribution experiences large changes when thermal expansions of the pad and shaft are included in the model. These changes may significantly affect film temperatures, local viscosities, and dynamic coefficients. The decreased film thickness causes a large increase in the stiffness and damping coefficients. This effect is increased as the operating speed increases. The pivot stiffness also has a significant effect on the dynamic coefficients and can be widely varied depending on its geometric parameters and type. In the results, it is difficult to distinguish which effect, thermal expansion or pivot flexibility, has a greater effect on the dynamic coefficients. However, it is clear that both effects are very important for accurately modeling TPJB dynamic force coefficients.

The use of the CFD-based approach presented for dynamic coefficient prediction appears to be justified for highly critical machines, based on the significant disparities between the CFD and Reynolds-MC predicted results provided here, and the uncertainty of the MCs. Future work will include developing hybrid

CFD-Reynolds models and reducing computation time since the present (walk clock) computation times are 14.4 h for the static solution, and 35.8 additional hours for the dynamic coefficient solution, using 12-cores of a computer server based on the dual Intel Xeon 2.5 GHz E5-2670 v2 10-core processors (TAMU High Performance Research Computing Center).

Acknowledgment

The authors gratefully acknowledge the funding received for this research from the Turbomachinery A&M Turbomachinery Research Consortium (TRC) and the Texas A&M High Performance Research Computing Center (HPRC).

Nomenclature

h = film thickness, m
k = turbulent kinetic energy, m^2/s^2
p = Pressure, Pa
r = volume faction
u = mean fluid velocity, m/s
R = radius, m
F = reaction force generated by fluid, N
M = reaction moment generated by fluid, Nm
T = temperature, °C
W = applied load, N
$\hat{\mathbf{c}}_{JJ}$ = synchronously reduced damping coefficient matrix
$\hat{\mathbf{k}}_{JJ}$ = synchronously reduced stiffness coefficient matrix
c_{ij} = damping coefficient, Ns/m
h_f = static enthalpy, J/kg
h_{tot} = mean total enthalpy, J/kg
k_{ij} = stiffness coefficient, N/m
p_e = pad pivot position at equilibrium, m
x_{se} = shaft x position at equilibrium, m
y_{se} = shaft y position at equilibrium, m
C_l = clearance, m
C_p = specific heat, J/kg K
F_{pvt} = reaction force generated by pivot, N
S_C = mass source per unit volume, kg/m^3
S_E = energy source per unit volume, J/m^3s
S_M = momentum source per unit volume, N/m^3
δ_e = pad tilting angle at equilibrium, deg
δ_{dec} = log decrement
Δh = film thickness displacement, m
Δp_e = pad pivot displacement at equilibrium, m
Δp_{pb} = pad perturbation pivot displacement at equilibrium, m
Δx = x mesh displacement at equilibrium, m
Δx_{pb} = shaft perturbation displacement in x-direction at equilibrium, m
Δx_{se} = shaft x displacement at equilibrium, m
Δy = y mesh displacement at equilibrium, m
Δy_{pb} = shaft perturbation displacement in y-direction at equilibrium, m
Δy_{se} = shaft y displacement at equilibrium, m
$\Delta\delta_e$ = pad tilting angular displacement at equilibrium, deg
$\Delta\delta_{pb}$ = pad perturbation angular displacement at equilibrium, m
θ_p = center angle of pad, deg
λ = thermal conductivity, W/mK
μ = dynamic viscosity, Pa s
ν = synchronous frequency, 1/s
ρ = density, kg/m^3
τ = molecular stress tensor, N/m^2
ω = turbulent frequency, 1/s
ω_s = rotating speed, rad/s
Ω = rotating speed, 1/s
$[c_{brg}]$ = full damping coefficient matrix
$[k_{brg}]$ = full stiffness coefficient matrix
$[m_{brg}]$ = full mass matrix
Pr = Prandtl number

Subscripts

0 = initial nodal position
eff = effective
f = fluid film
ibc = interface boundary
l = Liquid
p = pad (or pivot)
pvt = pivot
s = shaft
t = turbulent
$totp$ = total perturbation displacement
TE = thermal expansion
TEe = thermal expansion at equilibrium
v = vapor phase
α = vapor or liquid phase

Superscripts

j = pad number
$'$ = local coordinate

References

[1] Lund, J., 1964, "Spring and Damping Coefficients for the Tilting-Pad Journal Bearing," ASLE Trans., **7**(4), pp. 342–352.
[2] Knight, J. D., and Barrett, L. E., 1987, "Analysis of Tilting-Pad Journal Bearing With Heat Transfer Effects," ASME J. Tribol., **110**(1), pp. 128–133.
[3] Brugier, D., and Pascal, M. T., 1989, "Influence of Elastic Deformations of Turbo-Generator Tilting Pad Bearings on the Static Behavior and on the Dynamic Coefficients in Different Designs," ASME J. Tribol., **111**(2), pp. 364–371.
[4] Earles, L., Amentrout, R., and Palazzolo, A., 1990, "A Finite Element Approach to Pad Flexibility Effects in Tilt Pad Journal Bearings-Part I: Single Pad Analysis," ASME J. Tribol., **112**(2), pp. 169–176.
[5] Kim, J., Palazzolo, A., and Gadangi, R., 1995, "Dynamic Characteristics of TEHD Tilt Pad Journal Bearing Simulation Including Multiple Mode Pad Flexibility Model," ASME J. Vib. Acoust., **117**(1), pp. 123–135.
[6] Gadangi, R., and Palazzolo, A., 1995, "Transient Analysis of Tilt Pad Journal Bearings Including Effects of Pad Flexibility and Fluid Film Temperature," ASME J. Tribol., **117**(2), pp. 302–307.
[7] Desbordes, H., Wai, C. C. H., Fillon, M., and Frene, J., 1995, "The Effects of Three-Dimensional Pad Deformations on Tilting-Pad Journal Bearings Under Dynamic Loading," ASME J. Tribol., **117**(3), pp. 379–384.
[8] Suh, J., and Palazzolo, A. B., 2015, "Three-Dimensional Dynamic Model of TEHD Tilting-Pad Journal Bearing-Part I: Theoretical Modeling," ASME J. Tribol., **137**(4), p. 041704.
[9] Guo, Z., Toshio, H., and Gorden, R., 2005, "Application of CFD Analysis for Rotating Machinery Part1: Hydrodynamic, Hydrostatic Bearings and Squeeze Film Damper," ASME J. Eng. Gas Turbines Power, **4**, pp. 445–451.
[10] Meruane, V., and Pascual, R., 2008, "Identification of Nonlinear Dynamic Coefficients in Plain Journal Bearings," Tribol. Int., **41**(8), pp. 743–754.
[11] Liu, H., Xu, H., Ellison, P. J., and Jin, Z., 2010, "Application of Computational Fluid Dynamics and Fluid-Structure Interaction Method to the Lubrication Study of a Rotor-Bearing System," Tribol. Lett., **38**, pp. 324–336.
[12] Li, Q., Liu, S., Pan, X., and Zheng, S., 2012, "A New Method for Studying the 3D Transient Flow of Misaligned Journal Bearings in Flexible Rotor-Systems," J. Zhejiang Univ. Sci. A, **13**(4), pp. 293–310.
[13] Lin, Q., Wei, Z., Wang, N., and Chen, W., 2013, "Analysis on the Lubrication Performances of Journal Bearing System Using Computational Fluid Dynamics and Fluid-Structure Interaction Considering Thermal Influence and Cavitation," Tribol. Int., **64**, pp. 8–15.